ELSEVIER

Journal of Fluids and Structures 24 (2008) 336–365

JOURNAL OF FLUIDS AND STRUCTURES

www.elsevier.com/locate/jfs

# Boundary-integral modeling of cochlear hydrodynamics

C. Pozrikidis

*Department of Mechanical and Aerospace Engineering, University of California, San Diego, La Jolla, CA 92093-0411, USA*

Received 15 May 2006; accepted 20 August 2007
Available online 8 November 2007

**Abstract**

A two-dimensional model that captures the essential features of the vibration of the basilar membrane of the cochlea is proposed. The flow due to the vibration of the stapes footplate and round window is modeled by a point source and a point sink, and the cochlear pressure is computed simultaneously with the oscillations of the basilar membrane. The mathematical formulation relies on the boundary-integral representation of the potential flow established far from the basilar membrane and cochlea side walls, neglecting the thin Stokes boundary layer lining these surfaces. The boundary-integral approach furnishes integral equations for the membrane vibration amplitude and pressure distribution on the upper or lower side of the membrane. Several approaches are discussed, and numerical solutions in the frequency domain are presented for a rectangular cochlea model using different membrane response functions. The numerical results reproduce and extend the theoretical predictions of previous authors and delineate the effect of physical and geometrical parameters. It is found that the membrane vibration depends weakly on the position of the membrane between the upper and lower wall of the cochlear channel and on the precise location of the oval and round windows. Solutions of the initial-value problem with a single-period sinusoidal impulse reveal the formation of a traveling wave packet that eventually disappears at the helicotrema.


*Keywords:* Cochlear hydrodynamics; Membrane vibrations; Potential flow; Oscillatory flow

## 1. Introduction

The vibration of the eardrum due to external sound waves induces oscillations of the ossicular chain of the human middle ear consisting of three hinged bones: the malleus, the incus, and the stapes, as illustrated schematically in Fig. 1. The ossicular chain begins at the malleus, which is attached to the eardrum, and ends at the stapes footplate, which vibrates through the oval window into the inner ear. The amplitude of vibration is on the order of nanometers. The motion of the stapes footplate transmits pressure waves into the fluid-filled cochlea and thus activates the hearing nerves.

The snail-shaped human cochlea is a spiral tunnel with approximate radius 1 mm and approximate length 35 mm, housed in the temporal bone. The tunnel is divided along its length into three compartments: the upper scala vestibuli originating from the oval window, the lower scala tympani ending at the round window, and the intermediate scala media or cochlear duct, as shown in Fig. 1. The scala vestibuli and scala tympani are filled with perilymphatic fluid, which is a typical extracellular fluid with ionic composition comparable to that of cellular plasma. The cochlear duct is

*E-mail address:* cpozrikidis@ucsd.edu

0889-9746/$ - see front matter 
doi:10.1016/j.jfluidstructs.2007.08.006

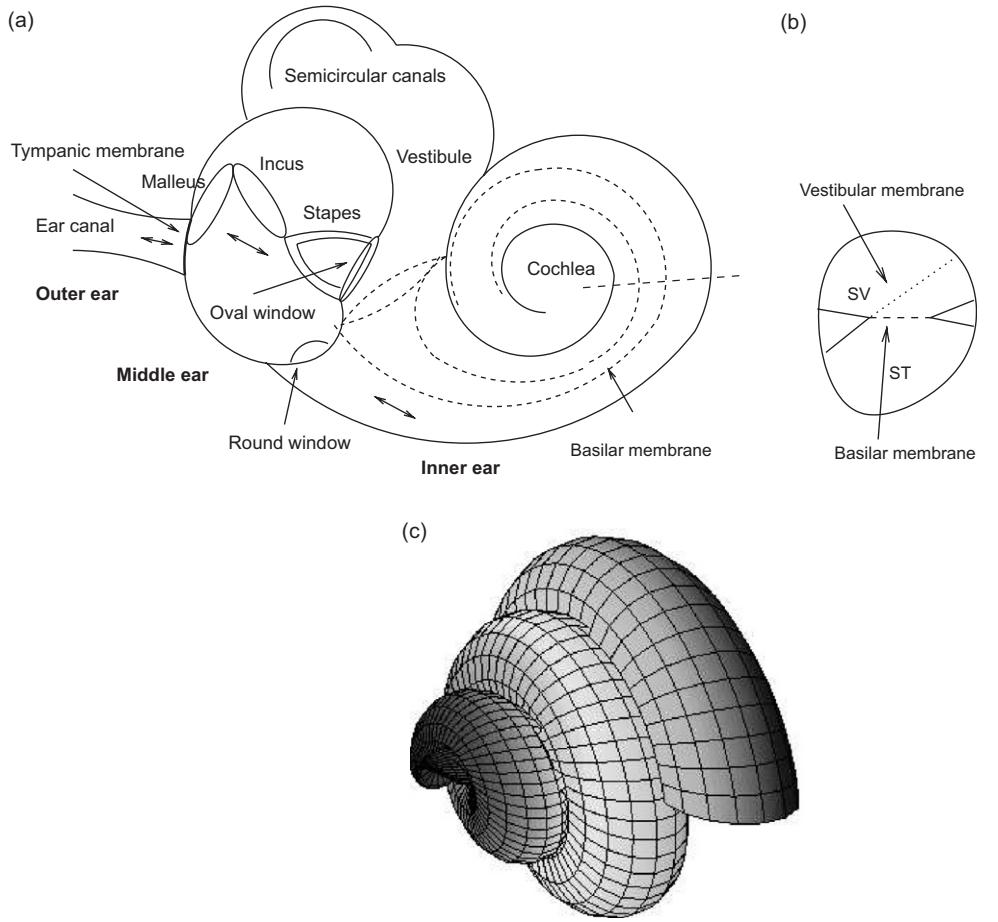


Fig. 1. (a) Schematic illustration of the outer, middle, and inner ear. The cochlea spirals outward from the plane of the illustration. The edges of the basilar membrane outlined with dashed lines are supported by the bony shelves. The width of the basilar membrane increases with distance into the cochlea. The basilar strip remains parallel to the plane of the illustration as it follows the cochlear turns. (b) Cross-section of the cochlear duct along the plane indicated with the bold faced, broken line in (a), indicating the scala vestibuli (SV) and the scala tympani (ST). The cochlear duct and vestibule contain endolymphatic fluid, whereas the scala vestibuli and scala tympani contain perilymphatic fluid. (c) Pictorial depiction of the snail-like cochlea generated using a mathematical expression and Matlab graphics. In the physical model considered in this paper, the cochlea is untwisted into a two-dimensional partitioned channel, yielding a two-dimensional configuration.

filled with endolymphatic fluid whose constitution is unlike that found elsewhere in the body. The three compartments meet at an opening located at the cochlea apex, called the helicotrema, across which perilymphatic fluid in the scala vestibuli and scala tympani communicate. The scala media is a narrow triangular duct occupying approximately 8% of the cochlear volume. It is separated from the scala vestibuli by the vestibular (Reissner's) membrane, and from the scala tympani by the basilar membrane. These membranes are elongated strips following the turns of the cochlea and supported on either side by the bony shelves consisting of the spiral lamina and spiral ligament. The anatomical features and dimensions cited here are specific to the human ear. Other mammals have different ossicular constructions, and only mammalian cochleas are coiled.

The organ of Corti is a sophisticated biological sensor attached to the basilar membrane and covered by the firmly fixed tectorial membrane. Vibrations of the basilar membrane due to pressure waves traveling through the cochlea induce rotational motions of the stereocilia pinned on the hair cells contained in the organ of Corti, and thereby open ion channels that activate the hearing nerves in a process described as mechanotransduction. The basilar membrane is narrow and stiff at the window end with a width of approximately 150 μm, and wide and flexible at the apical end with a width of approximately 560 μm. Although the membrane widens toward the helicotrema, the duct becomes more

narrow. The non-uniformity of the membrane stiffness is responsible for different regions vibrating at different frequencies along the length of the cochlea. The beginning of the membrane near the stapes vibrates at high frequencies, while the apical end vibrates at low frequencies. The membrane thus acts as a spatial frequency analyzer. Consequently, local injury or acoustic trauma results in hearing loss in a certain frequency bandwidth.

Modeling the function of the cochlea has a long record in the medical, physiological, engineering, and mathematical literature. Theoretical studies date back to the pioneering work of Helmholtz who treated the basilar membrane as a tapered elastic sheet, ignoring the effect of fluid flow. In most theoretical studies, the cochlea is modeled as a two-compartment system where the scala vestibuli and the scala tympani are separated by the basilar membrane. Because of the small thickness and low resistance to bending, Reissner's membrane is assumed to be convected passively with the flow. Early one-dimensional transmission models either neglected or adopted heuristic approximations for the fluid pressure on either side of the membrane. Phenomenological models have emulated the action of the membrane in terms of a one-dimensional impedance which either complements or is embedded in the equation of fluid motion.

Because of the prevailing opinion that the spiral shape of the cochlea is not acoustically significant [e.g., Viergever (1978), Loh (1983), Steele and Zais (1985), Manoussaki and Chadwick (2000)], the vast majority of theoretical models have addressed the function of the unwrapped cochlea mapped to the rectangular partitioned channel. However, recent studies have shown that the cochlear curvature enhances the radial shearing in the region of the basilar membrane where low-frequency sounds are analyzed (Cai et al., 2005; Manoussaki et al., 2006). Since viscous fluid stresses are confined inside narrow boundary layers lining the cochlear walls and basilar membrane, the fluid motion is typically described in terms of the equations of potential flow with the pressure gradient acting as the driving force, as will be discussed in Section 2. Tackling the problem in the more general context of Navier–Stokes flow requires the resolution of thin boundary layers and demands exorbitant computational time (Givelberg and Bunn, 2003).

Numerical solutions of two-dimensional cochlear models were presented by several authors including Lesser and Berkley (1972), Viergever and Kalker (1975), Viergever (1977), Allen (1977), Sondhi (1978), Allen and Sondhi (1979), Neely (1981), Kagawa et al. (1987), Diependaal and Viergever (1989), and Beyer (1992). Prior to Lesser and Berkley (1972), all authors had assumed that the fluid motion is one-dimensional. Lighthill (1981) used energy-flow arguments to identify the necessary key features of mathematical models. Numerical solutions of three-dimensional cochlear models were presented by Taber and Steele (1981), Kagawa et al. (1987), Kolston and Ashmore (1996), Parthasarathi et al. (2000) and Givelberg and Bunn (2003). The governing equations were solved using integral formulations, finite difference, finite element, and immersed boundary methods. Kagawa et al. (1987) performed three-dimensional simulations of the fluid motion inside a spiraling cochlea and confirmed that the results are in qualitative agreement with those of simpler two-dimensional geometries.

In this paper, a two-dimensional model is proposed that captures the essential features of vibration of the basal membrane and can be tackled accurately and efficiently by elementary numerical methods. Conceptually, the model is similar to that considered by Neely (1981) and earlier authors, with some differences. The main idea is to represent the flow due to the vibration of the stapes footplate and membrane of the round window in terms of a point source and a point sink, and then solve for the cochlear pressure while simultaneously computing the oscillations of the basilar membrane. The problem formulation relies on the boundary-integral method for the potential flow established far from the basilar membrane and cochlea side walls. One key objective of the boundary-integral formulation is the derivation of an integral equation defined over the domain of interest alone, in this case the basilar membrane. This is accomplished by using of a point source and a point sink, and then introducing Green's functions of the second kind (Neumann functions) to satisfy the no-penetration condition over the surrounding surfaces. For simple geometries, the Green's function is available in analytical form. This approach circumvents a great deal of numerical noise due to the discretization of cochlear surfaces, including corners and regions where discontinuous velocities are specified. The end-result is a system of integral equations for the membrane vibration amplitude and pressure distribution on the upper or lower side of the membrane.

In Section 2, the hydrodynamics of the cochlea is summarized, and the governing differential equations are derived. A general integral formulation employing the point source/sink model for a two-dimensional cochlea with arbitrary geometry is discussed in Section 3. In Section 4, a more specific model consisting of two rectangular compartments is considered. Using the Neumann function of Laplace's equation for a semi-infinite strip, weakly singular integral equations with logarithmic kernels and hypersingular integral equations defined over the length of the basilar membrane are derived using alternative formulations. Allen (1977), Sondhi (1978), and Allen and Sondhi (1979) developed similar formulations based on a serial model proposed by Lesser and Berkley (1972), as discussed in Section 5. In their model, the two cochlear compartments are unwrapped and put serially next to one another as if they were hinged at the helicotrema. In Section 6, a more general formulation applicable to a closed cochlea in the presence of the helicotrema is derived in terms of a composite Green's function generated by a point source and a point sink with equal

and opposite strengths in a rectangular domain. In Section 7, numerical methods for solving the derived integral equations are discussed.

In Section 8, numerical solutions are presented and discussed in the frequency domain, and in Section 9, the initial-value problem is considered where the flow is driven by an arbitrary impulse. The transient response of the basilar membrane is examined, and the establishment of a periodic oscillation under constant sinusoidal forcing is described. The results show that the transient motion exhibits an interesting dynamics that complements the periodic motion observed under harmonic excitation.

## 2. Cochlear hydrodynamics

We consider oscillatory flow in the cochlea generated by the harmonic vibration of the stapes footplate with amplitude $\varepsilon$ and frequency $f$, in the human physiological range of 20–20 000 Hz. Under physiological conditions, $\varepsilon$ is on the order of nanometers. The vibration induces perilymphatic flow, and the associated pressure field transmits pressure waves into the cochlea that activate the sensory hair cells located in the organ of Corti.

The perilymph can be assumed to be an incompressible Newtonian fluid whose motion is governed by the Navier–Stokes equation

$$\rho\left(\frac{\partial \mathbf{u}}{\partial t}+\mathbf{u}\cdot\nabla\mathbf{u}\right)=-\nabla p+\mu\nabla^2\mathbf{u}, \tag{1}$$

and the continuity equation

$$\nabla\cdot\mathbf{u}=0, \tag{2}$$

where $\mathbf{u}$ is the fluid velocity, $p$ is the fluid pressure, $\rho$ is the fluid density, and $\mu$ is the fluid viscosity [e.g., Pozrikidis (1997)]. The assumption of incompressibility is justified at all but the highest frequencies in the physiological range. At 20 kHz, the wavelength of the longitudinal acoustic wave is around 75 mm, which is only twice the length of the cochlea.

The magnitude of the velocity of the flow induced by the vibration of the stapes footplate is $V=\omega\varepsilon$, and the characteristic time scale is $1/\omega$, where $\omega=2\pi f$ is the angular frequency. The volumetric flow rate (volume velocity) induced by the footplate displacement is the product of the displacement velocity, $V$, and footplate cross-sectional area, $A\simeq 3.2\,\mathrm{mm}^2$. The Reynolds number of the flow expresses the relative importance of inertial-convective and viscous fluid forces,

$$\mathrm{Re}\equiv\frac{\rho VL}{\mu}=\frac{\rho\omega\varepsilon L}{\mu}, \tag{3}$$

where $L\simeq 3.5\,\mathrm{cm}$ is the length of the basilar membrane. The dimensionless frequency parameter

$$\beta\equiv\frac{\rho\omega L^2}{\mu} \tag{4}$$

expresses the relative importance of inertial-unsteady and viscous forces. The Strouhal number expresses the relative importance of inertial-unsteady and inertial-acceleration forces,

$$\mathrm{St}\equiv\frac{\beta}{\mathrm{Re}}=\frac{fL}{V}=\frac{L}{\varepsilon}. \tag{5}$$

Because the amplitude of the stapes footplate vibration is small, $\varepsilon\ll L$, the Strouhal number is high, and the Navier–Stokes equation may be linearized to yield the unsteady Stokes equation

$$\rho\frac{\partial \mathbf{u}}{\partial t}=-\nabla p+\mu\nabla^2\mathbf{u}. \tag{6}$$

To study pure-tone hydrodynamics, we set

$$\mathbf{u}=\mathbf{U}\exp(\mathrm{i}\omega t),\quad p=P\exp(\mathrm{i}\omega t), \tag{7}$$

where i is the imaginary unit, $\mathbf{U}$ is the velocity amplitude, and $P$ is the pressure amplitude. Substituting in the unsteady Stokes equation we derive the complex Brinkman equation,

$$\mathrm{i}\omega\rho\mathbf{U}=-\nabla P+\mu\nabla^2\mathbf{U}, \tag{8}$$

complemented by the continuity equation for an incompressible fluid,

$$\nabla \cdot \mathbf{U} = 0, \tag{9}$$

to be solved subject to appropriate boundary conditions. Using the incompressibility condition, we find that the pressure is a harmonic function,

$$\nabla^2 P = 0. \tag{10}$$

At high frequencies, the flow is comprised a thin Stokes boundary layer and an outer potential flow. The thickness of the Stokes boundary layer is

$$\delta = \sqrt{\frac{\nu}{\omega}} = \sqrt{\frac{\nu}{2\pi f}}, \tag{11}$$

where $\nu = \mu/\rho$ is the kinematic viscosity of the fluid. Taking $\nu = 1\,\text{mm}^2/\text{s}$, we find that, as the frequency $f$ increases from 20 to 20 000 Hz, $\delta$ decreases from 0.089 to 0.0028 mm, and is thus smaller than the radius of the cochlear duct ($\sim$1.0 mm). The flow outside the boundary layer is governed by the simplified equation

$$\rho \frac{\partial \mathbf{u}}{\partial t} = -\nabla p. \tag{12}$$

Substituting (7) and rearranging, we find

$$\mathbf{U} = \frac{\mathrm{i}}{\omega\rho} \nabla P, \tag{13}$$

which shows that the velocity oscillation lags the pressure oscillation by $-90^\circ$. The no-penetration boundary condition requires

$$\mathbf{n} \cdot \nabla P = -\mathrm{i}\omega\rho \mathbf{n} \cdot \mathbf{U}_w \tag{14}$$

at the edge of the Stokes boundary layer, where $\mathbf{U}_w$ is the wall velocity and $\mathbf{n}$ is the unit normal vector. This expression shows that, given the amplitude of the footplate velocity, the amplitude of the pressure increases linearly with frequency.

In the remainder of this paper, we consider the potential flow established in the cochlea outside the Stokes boundary layer. The precise effect of the fluid viscosity was discussed by several previous authors using asymptotic and numerical methods [e.g., LeVeque et al. (1988), Cai et al. (2005)]. In the potential-flow model, viscous dissipation is implemented through a damping coefficient in the membrane response function.

## 3. A two-dimensional cochlear model

Fig. 2(a) illustrates a two-dimensional model that arises by untwisting the spiral cochlea around the $y$ axis. The cross-section of the basilar membrane, shown as a bold line along its length, separates the scala vestibuli (upper compartment) from the scala tympani (lower compartment). The $xy$ plane in Fig. 2(a) is perpendicular to the plane of the schematic illustration in Fig. 1(b). The $x$ axis points along the length of the basilar membrane, and the $y$ axis points normal to the basilar membrane.

In the proposed theoretical model, the vibration of the stapes footplate is mediated by an oscillatory point source of strength (volume velocity) $Q$. The induced pressure and velocity amplitudes in the $xy$ plane are described by

$$P_{src} = \mathrm{i}\omega\rho Q G(\mathbf{x}, \mathbf{x}_{src}), \quad \mathbf{U}_{src} = -Q \nabla G(\mathbf{x}, \mathbf{x}_{src}), \tag{15}$$

where $G(\mathbf{x}, \mathbf{x}_{src})$ is the Green's function of the two-dimensional Laplace equation representing the potential of the flow due to a point sink; the free-space Green's function is $G(\mathbf{x}, \mathbf{x}_0) = -(1/2\pi)\log|\mathbf{x} - \mathbf{x}_0|$. The strength of the point source is $Q = \omega\varepsilon d$, where $\varepsilon$ is the amplitude of the stapes footplate displacement, and $d$ is the effective footplate diameter. It is sensible to approximate $d = A/b$, and thus obtain $Q = \omega\varepsilon A/b$, where $A$ the stapes footplate area and $b$ is the cochlea channel width. Similarly, the action of the round window is represented by an oscillating point sink with strength $-Q$. The induced pressure and velocity fields are

$$P_{\text{sink}} = -\mathrm{i}\omega\rho Q G(\mathbf{x} - \mathbf{x}_{\text{sink}}), \quad \mathbf{U}_{\text{sink}} = Q \nabla G(\mathbf{x} - \mathbf{x}_{\text{sink}}). \tag{16}$$

Note that the strength of the point sink is equal in magnitude and opposite in sign to that of the point source, as the incompressible fluid cannot escape through side walls. The no-penetration boundary condition requires that the normal

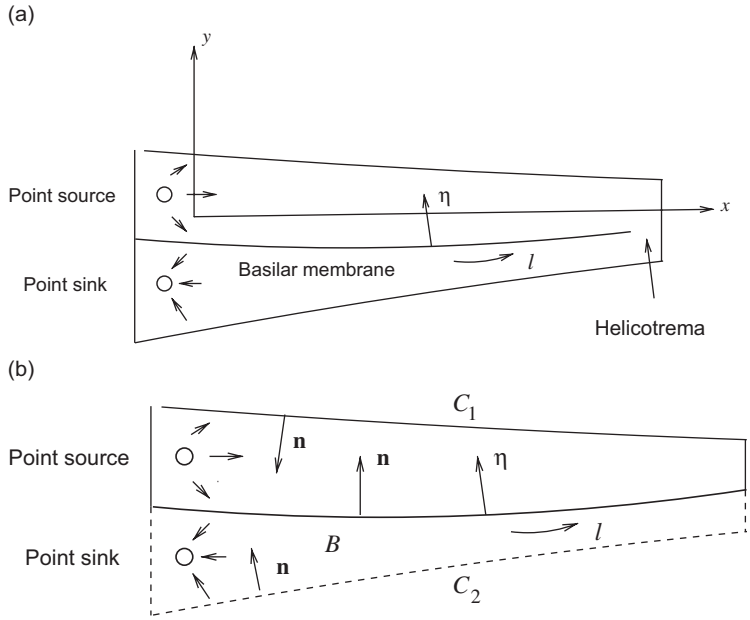


Fig. 2. (a) A two-dimensional model arises by untwisting the spiral cochlea. The action of the stapes footplate and round window are emulated, respectively, by a point source and a point sink. (b) Boundary contours for developing the boundary-integral formulation; the contour $C_1$ is drawn as a solid line, and the contour $C_2$ is drawn as a broken line.

component of the velocity is zero, and thus the normal derivative of the pressure vanishes around the cochlear walls, $\mathbf{n}\cdot\nabla P = 0$.

In most previous models, the oval and round windows are assumed to occupy, respectively, the upper and lower portions of the left wall separated by the basilar membrane, both vibrating in a piston-like fashion with a uniform velocity [e.g., Kagawa et al. (1987)].

The transverse displacement of the basilar membrane is described by the function $\eta = f(l,t)$, where $l$ is the arc length along the undisturbed position of the basilar membrane, and $\eta$ is the normal distance, as shown in Fig. 2. For oscillatory flow,

$$f(l,t) = F(l)\exp(\mathrm{i}\omega t). \tag{17}$$

A real amplitude $F(l)$ describes a stationary wave, and a complex amplitude $F(l)$ describes a traveling wave. Requiring the kinematic condition

$$\frac{\partial f}{\partial t} = \mathbf{n}\cdot\mathbf{u}, \tag{18}$$

at $\eta = 0$, we find

$$\mathrm{i}\omega F = \frac{\mathrm{i}}{\omega\rho}\frac{\partial P}{\partial \eta} \tag{19}$$

at $\eta = 0$, where the normal pressure derivative is evaluated on either side of the basilar membrane. Rearranging, we find

$$\frac{\partial P}{\partial \eta} = \rho\omega^2 F. \tag{20}$$

If we assume that fluid does not enter the helicotrema, we may require area conservation in the upper or lower compartment expressed by

$$Q\exp(\mathrm{i}\omega t) = -\frac{\mathrm{d}}{\mathrm{d}t}\int f(l,t)\,\mathrm{d}l, \tag{21}$$

where the integral is computed along the undisturbed position of the basilar membrane. Substituting (17) and simplifying, we derive the integral constraint

$$\int F(l)\mathrm{d}l = \mathrm{i}\frac{Q}{\omega}. \tag{22}$$

Next, we balance the pressure on either side of the basilar membrane with the restoring elastic and viscous membrane tension and viscous fluid stresses, finding

$$[p](l) = -\mathscr{C}(f, f_{ll}, f_{llll}, f_t, f_{tt}), \tag{23}$$

where $[p] \equiv p(\eta = 0+) - p(\eta = 0-)$ denotes the pressure jump across the membrane, $\mathscr{C}$ is a membrane response function, and a subscript denotes a derivative with respect to the corresponding variable. The second and fourth derivatives with respect to $l$ arise by modeling the membrane as a von Kármán elastic plate [e.g., Allen and Sondhi (1979)]. The second derivative with respect to time expresses the effect of the membrane inertia.

### 3.1. Membrane response function

Several membrane response functions have been employed by previous authors. One possible choice is

$$\mathscr{C} = s_0 \mathrm{e}^{-\lambda(l-l_r)}(f + \beta f_t), \tag{24}$$

where $s_0$ is a constant coefficient, $\lambda$ is a viscous decay coefficient, $l_r$ is a reference position, and $\beta$ is a dissipation coefficient expressing the effect of fluid and membrane viscosities (LeVeque et al., 1985, 1988). In this model, the membrane mass is neglected on the observation that draining the cochlear fluid drastically alters the response of the basilar membrane by eliminating the spatial resonance discussed in the Introduction. An alternative interpretation is that the density of the cochlea fluid plays an important role. In fact, our computations will show that the membrane mass is an important determinant of the membrane vibration. Substituting the preceding expressions, we obtain

$$[P] = -s_0 \mathrm{e}^{-\lambda(l-l_r)}(1 + \mathrm{i}\omega\beta)F(l). \tag{25}$$

More generally, we write

$$[P] = -\mathscr{F}(l, \omega)F(l), \tag{26}$$

where $\mathscr{F}(l, \omega)$ is a position- and frequency-dependent transfer function, and $\mathscr{F}(l, \omega)/(\mathrm{i}\omega)$ is the specific acoustic impedance. In the case of (25),

$$\mathscr{F}(l, \omega) = s_0 \mathrm{e}^{-\lambda(l-l_r)}(1 + \mathrm{i}\omega\beta). \tag{27}$$

A general membrane response function is

$$\mathscr{C} = c(l)f + \kappa(l)f_t + m(l)f_{tt}, \tag{28}$$

corresponding to

$$\mathscr{F}(l, \omega) = c(l) + \mathrm{i}\omega\kappa(l) - \omega^2 m(l), \tag{29}$$

where $c(l)$ is the membrane stiffness, $\kappa(l)$ is the viscous resistance coefficient, and $m(l)$ is the membrane areal mass density [e.g., Kagawa et al. (1987)]. These authors found that the membrane stiffness and mass determine the peak position of the frequency response, while the viscous resistance determines the sharpness of the response peak.

The total pressure field in the cochlea is given by the linear superposition

$$P = P_{src} + P_{snk} + P', \tag{30}$$

or

$$P = \mathrm{i}\omega\rho Q(G(\mathbf{x}, \mathbf{x}_{src}) - G(\mathbf{x}, \mathbf{x}_{snk})) + P', \tag{31}$$

where the nonsingular pressure, $P'$, is introduced to satisfy the boundary conditions over the cochlear walls. The problem has been reduced to solving Laplace's equation

$$\nabla^2 P' = 0, \tag{32}$$

in the scala vestibuli and scala tympani, and simultaneously computing the membrane amplitude function, $F(l)$, subject to the no-penetration condition

$$\mathbf{n}\cdot\nabla P' = -\mathbf{n}\cdot\nabla(P_{src}+P_{snk}) = -\mathrm{i}\omega\rho Q\mathbf{n}\cdot\nabla(G(\mathbf{x},\mathbf{x}_{src})-G(\mathbf{x},\mathbf{x}_{snk})) \tag{33}$$

around the cochlear walls. The kinematic condition at the basilar membrane requires

$$\frac{\partial P'}{\partial\eta} = \rho\omega^2 F - \frac{\partial P_{src}}{\partial\eta} - \frac{\partial P_{snk}}{\partial\eta} = \rho\omega^2 F - \mathrm{i}\rho\omega Q\frac{\partial}{\partial\eta}(G(\mathbf{x},\mathbf{x}_{src})-G(\mathbf{x},\mathbf{x}_{snk})), \tag{34}$$

and the dynamic condition requires

$$[P'] = -\mathscr{F}(l,\omega)F(l), \tag{35}$$

evaluated at $\eta = 0$.

### 3.2. Boundary-integral formulation

Several boundary-integral formulations are possible reflecting different various geometrical simplifications at the helicotrema. In one approach, the presence of the helicotrema is altogether neglected, as shown in Fig. 2(b). Consider a point $\mathbf{x}_0$ inside the scala vestibuli. Green's third identity provides us with the boundary-integral representation

$$P'(\mathbf{x}_0) = -\int_{C_1,B} G(\mathbf{x},\mathbf{x}_0)\mathbf{n}(\mathbf{x})\cdot\nabla P'(\mathbf{x})\,\mathrm{d}l(\mathbf{x}) + \int_{C_1,B} P'(\mathbf{x})\mathbf{n}(\mathbf{x})\cdot\nabla G(\mathbf{x},\mathbf{x}_0)\,\mathrm{d}l(\mathbf{x}), \tag{36}$$

where $B$ stands for the basilar membrane, $C_1$ stands for the cochlear walls bounding the scala vestibuli drawn with the solid line in Fig. 2(b), $G(\mathbf{x},\mathbf{x}_0)$ is the free-space Green's function of Laplace's equation in two dimensions, and the normal vector $\mathbf{n}$ over $C_1$ and $B$ points into the scala vestibuli, as illustrated in Fig. 2(b) [e.g., Pozrikidis, 2002]. The first integral on the right-hand side of (36) is the single-layer potential, and the second integral is the double-layer potential of potential flow.

Similarly, we write the reciprocal relation

$$0 = -\int_{C_2,B} G(\mathbf{x},\mathbf{x}_0)\mathbf{n}(\mathbf{x})\cdot\nabla P'(\mathbf{x})\,\mathrm{d}l(\mathbf{x}) + \int_{C_2,B} P'(\mathbf{x})\mathbf{n}(\mathbf{x})\cdot\nabla G(\mathbf{x},\mathbf{x}_0)\,\mathrm{d}l(\mathbf{x}), \tag{37}$$

where $C_2$ stands for the cochlear walls bounding the scala tympani drawn with the broken line in Fig. 2(b), and the normal vector $\mathbf{n}$ points into the scala tympani, as illustrated in Fig. 2(b). Adding these equations and observing that the normal component of the velocity and therefore the normal component of the pressure gradient is continuous across $B$, we obtain

$$\begin{aligned} P'(\mathbf{x}_0) = &-\int_{C_1,C_2} G(\mathbf{x},\mathbf{x}_0)\mathbf{n}(\mathbf{x})\cdot\nabla P'(\mathbf{x})\,\mathrm{d}l(\mathbf{x}) + \int_{C_1,C_2} P'(\mathbf{x})\mathbf{n}(\mathbf{x})\cdot\nabla G(\mathbf{x},\mathbf{x}_0)\,\mathrm{d}l(\mathbf{x}) \\ &+ \int_B [P'](\mathbf{x})\mathbf{n}(\mathbf{x})\cdot\nabla G(\mathbf{x},\mathbf{x}_0)\,\mathrm{d}l(\mathbf{x}), \end{aligned} \tag{38}$$

where the normal vector over $B$ in the last integral points into the scala vestibuli. Exactly the same expression arises when the point $\mathbf{x}_0$ lies inside the scala tympani.

Now we take the limit of (36) as the field point $\mathbf{x}_0$ approaches $C_1$ or $B$, and note that the double-layer potential undergoes a discontinuity due to the distributed potential dipoles. The limiting value of the double-layer potential can be expressed in terms of the readily computable principal value using the integral identity

$$\lim_{\mathbf{x}\to C_1,B}\int_{C_1,B} P'(\mathbf{x})\mathbf{n}(\mathbf{x})\cdot\nabla G(\mathbf{x},\mathbf{x}_0)\,\mathrm{d}l(\mathbf{x}) = \frac{1}{2}P'(\mathbf{x}_0) + \fint_{C_1,B} P'(\mathbf{x})\mathbf{n}(\mathbf{x})\cdot\nabla G(\mathbf{x},\mathbf{x}_0)\,\mathrm{d}l(\mathbf{x}), \tag{39}$$

where $\fint$ denotes the principal value integral [e.g., Pozrikidis (2002)]. Thus, we find

$$\frac{1}{2}P'(\mathbf{x}_0^{SV}) = -\int_{C_1,B} G(\mathbf{x},\mathbf{x}_0)\mathbf{n}(\mathbf{x})\cdot\nabla P'(\mathbf{x})\,\mathrm{d}l(\mathbf{x}) + \fint_{C_1,B} P'(\mathbf{x})\mathbf{n}(\mathbf{x})\cdot\nabla G(\mathbf{x},\mathbf{x}_0)\,\mathrm{d}l(\mathbf{x}), \tag{40}$$

and $SV$ denotes the scala vestibuli. Taking also the limit of (38) as $\mathbf{x}_0$ tends to the basilar membrane and following a similar procedure, we find

$$P'(\mathbf{x}_0^{SV}) = -\int_{C_1,C_2} G(\mathbf{x},\mathbf{x}_0)\mathbf{n}(\mathbf{x})\cdot\nabla P'(\mathbf{x})\,\mathrm{d}l(\mathbf{x}) + \int_{C_1,C_2} P'(\mathbf{x})\mathbf{n}(\mathbf{x})\cdot\nabla G(\mathbf{x},\mathbf{x}_0)\,\mathrm{d}l(\mathbf{x}) + \frac{1}{2}[P'](\mathbf{x}_0) + \text{⨍}\!\!\!\!\!\!-\!\!\!\!\!\!\int_B [P'](\mathbf{x})\mathbf{n}(\mathbf{x})\cdot\nabla G(\mathbf{x},\mathbf{x}_0)\,\mathrm{d}l(\mathbf{x}). \tag{41}$$

Finally, taking the limit of (38) as $\mathbf{x}_0$ tends to $C_2$, we find

$$\frac{1}{2}P'(\mathbf{x}_0^{ST}) = -\int_{C_1,C_2} G(\mathbf{x},\mathbf{x}_0)\mathbf{n}(\mathbf{x})\cdot\nabla P'(\mathbf{x})\,\mathrm{d}l(\mathbf{x}) + \text{⨍}\!\!\!\!\!\!-\!\!\!\!\!\!\int_{C_1,C_2} P'(\mathbf{x})\mathbf{n}(\mathbf{x})\cdot\nabla G(\mathbf{x},\mathbf{x}_0)\,\mathrm{d}l(\mathbf{x}) + \int_B [P'](\mathbf{x})\mathbf{n}(\mathbf{x})\cdot\nabla G(\mathbf{x},\mathbf{x}_0)\,\mathrm{d}l(\mathbf{x}), \tag{42}$$

where $ST$ denotes the scala tympani. Implementing the boundary conditions, we derive a system of integral equations for the pressure distribution along the cochlea walls and membrane shape function, $F(l)$.

The complexity of this formulation motivates the development of rectangular cochlear models reflecting different physical assumptions at the downstream end located at the helicotrema, discussed in the next three sections.

## 4. Semi-infinite cochlear model

Fig. 3 illustrates a rectangular cochlear model with $l = x$ and $\eta = y$. The upper wall is located at $y = a$, the lower wall is located at $y = -a$, the basilar membrane is located at $y = y_b$, the left vertical wall is located at $x = 0$, and the right vertical wall is located at $x = L$. The total height of the cochlear channel is $h = 2a$. The point source and point sink are located at arbitrary positions near the left vertical wall. Typical physiological values are $a = 0.1$ cm, $h = 0.2$ cm and $L = 3.5$ cm, corresponding to aspect ratio $L/h = 17.5$.

To model the flow, we use the boundary-integral representation discussed in Section 3. Since both pressure and velocity decay with distance into the cochlea at sufficiently high frequencies, the integral along the far side of the cochlea near the helicotrema can be neglected to a leading-order approximation, leading us to the semi-infinite cochlea model.

To further simplify the analysis, we introduce a Green's function of the second kind, also called a Neumann function, that satisfies the no-penetration condition $\mathbf{n}(\mathbf{x})\cdot\nabla G(\mathbf{x},\mathbf{x}_0) = 0$ when $\mathbf{x}$ is on the left, upper, and lower side of the cochlea wall. Physically, the Green's function represents the velocity potential (pressure field) due to a point sink located at the point $\mathbf{x}_0$ in a semi-infinite strip confined between two horizontal walls located at $y = w_1$, $y = w_2 > w_1$, and a vertical wall

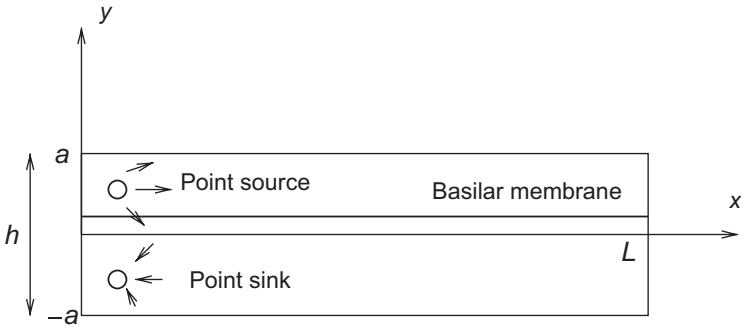


Fig. 3. Illustration of a two-dimensional rectangular cochlea model. The longitudinal cross-section of the basilar membrane is drawn as a bold horizontal line.

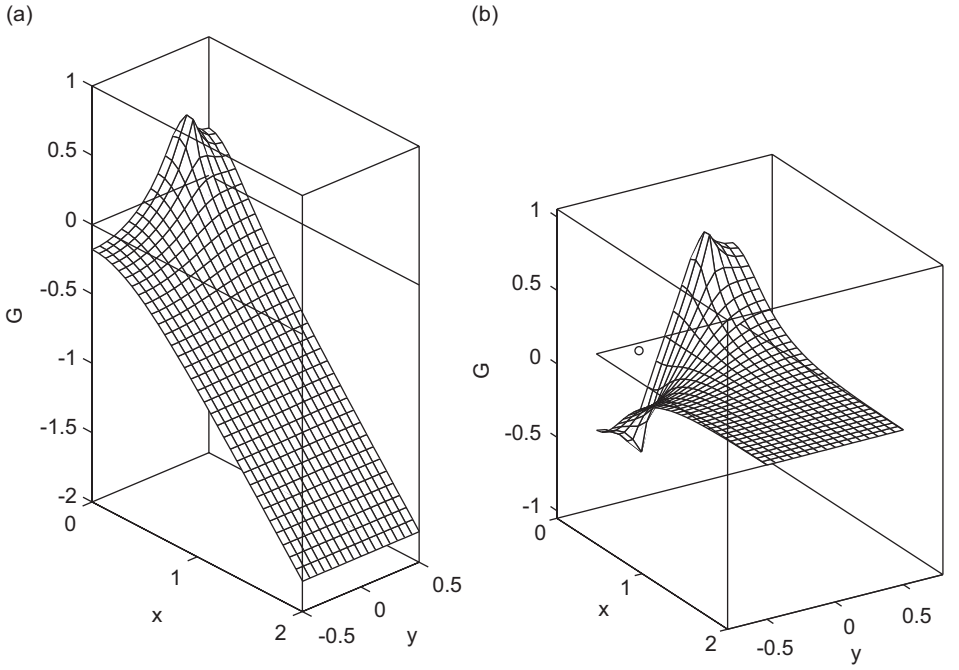


Fig. 4. (a) Green's function in a semi-infinite strip confined between three walls representing the pressure field due to a point sink of unit strength. (b) Pressure field due to a point source/sink pair in a semi-infinite strip. The fields become infinite at the singular points.

located at $x = w_3$. In our case, $w_1 = -a$, $w_2 = a$, and $w_3 = 0$. Using the method of images, we find

$$\begin{aligned} G_{w_1,w_2,w_3}(\mathbf{x},\mathbf{x}_0) = & -\frac{1}{4\pi}\log\left[\left(\cosh\frac{\pi(x-x_0)}{h}-\cos\frac{\pi(y-y_0)}{h}\right)\times\left(\cosh\frac{\pi(x-x_0)}{h}-\cos\frac{\pi(y+y_0-2w_1)}{h}\right)\right] \\ & -\frac{1}{4\pi}\log\left[\left(\cosh\frac{\pi(x+x_0-2w_3)}{h}-\cos\frac{\pi(y-y_0)}{h}\right)\right. \\ & \left.\times\left(\cosh\frac{\pi(x+x_0-2w_3)}{h}-\cos\frac{\pi(y+y_0-2w_1)}{h}\right)\right], \end{aligned} \tag{43}$$

where $h = w_2 - w_1$ [e.g., Pozrikidis (2002)]. It can be confirmed by direct substitution that this Green's function satisfies the boundary conditions $\partial G(\mathbf{x},\mathbf{x}_0)/\partial y = 0$ when $y = w_1, w_2$, and $\partial G(\mathbf{x},\mathbf{x}_0)/\partial x = 0$ when $x = w_3$. The first logarithmic term on the right-hand side of (43) represents the image system for the two horizontal parallel walls, and the second logarithmic term represents the reflection of the image system with respect to the vertical wall. Fig. 4(a) shows a graph of the Green's function, revealing the expected linear increase with distance along the strip corresponding to a uniform flow with a flat velocity profile. Fig. 4(b) shows the $c$ potential field due to a point source and a point sink with equal strengths, revealing a rapid exponential decay with distance along the strip. For convenience, the subscripts $w_1, w_2, w_3$ will be suppressed in the following discussion.

With this Green's function, the integral representations (36) and (38) simplify to

$$P'(\mathbf{x}_0) = -\int_0^L G(\mathbf{x},\mathbf{x}_0)\frac{\partial P'}{\partial y}(x)\,\mathrm{d}x + \int_0^L P'(x)\frac{\partial G(\mathbf{x},\mathbf{x}_0)}{\partial y}\,\mathrm{d}x \tag{44}$$

and

$$P'(\mathbf{x}_0) = \int_0^L [P'](x)\frac{\partial G(\mathbf{x},\mathbf{x}_0)}{\partial y}\,\mathrm{d}x, \tag{45}$$

where the integrals are computed along the length of the basilar membrane located at $y = y_b$. Eq. (45) expresses the pressure field as a distribution of potential dipoles oriented normal to the undisturbed membrane.

Taking the limit of (44) and (45) as the field point $\mathbf{x}_0$ tends to the basilar membrane from the upper side, and expressing the limit in terms of the principal value using (39), we find

$$\frac{1}{2}P'(x_0) = -\int_0^L G(\mathbf{x},\mathbf{x}_0)\frac{\partial P'}{\partial y}(x)\,\mathrm{d}x + \fint_0^L P'(x)\frac{\partial G(\mathbf{x},\mathbf{x}_0)}{\partial y}\,\mathrm{d}x \tag{46}$$

and

$$P'(x_0) = \frac{1}{2}[P'](x_0) + \fint_0^L [P'](x)\frac{\partial G(\mathbf{x},\mathbf{x}_0)}{\partial y}\,\mathrm{d}x. \tag{47}$$

Next, we substitute in (46) the kinematic boundary condition (34), and in (47) the dynamic boundary condition (35), and find

$$\begin{aligned}\frac{1}{2}P'(x_0) = &-\rho\omega^2\int_0^L G(\mathbf{x},\mathbf{x}_0)F(x)\,\mathrm{d}x + \mathrm{i}\omega\rho Q\int_0^L G(\mathbf{x},\mathbf{x}_0)\frac{\partial}{\partial y}(G(\mathbf{x},\mathbf{x}_{src}) - G(\mathbf{x},\mathbf{x}_{snk}))\,\mathrm{d}x \\ &+ \fint_0^L P'(x)\frac{\partial G(\mathbf{x},\mathbf{x}_0)}{\partial y}\,\mathrm{d}x\end{aligned} \tag{48}$$

and

$$P'(x_0) = -\frac{1}{2}\mathscr{F}(x_0,\omega)F(x_0) - \fint_0^L \mathscr{F}(x,\omega)F(x)\frac{\partial G(\mathbf{x},\mathbf{x}_0)}{\partial y}\,\mathrm{d}x. \tag{49}$$

The last two equations are to be solved for the amplitude, $F(x)$, and for the pressure distribution on the upper surface of the basilar membrane, $P'(x)$.

Now substituting $Q = \omega\varepsilon d$ and rearranging, we derive the dimensionless forms of (48) and (49),

$$\int_0^{\hat{L}} G(\mathbf{x},\mathbf{x}_0)\zeta(x)\,\mathrm{d}\hat{x} + \frac{1}{2}\hat{P}'(x_0) - \fint_0^{\hat{L}} \hat{P}'(x)\frac{\partial G(\mathbf{x},\mathbf{x}_0)}{\partial \hat{y}}\,\mathrm{d}\hat{x} = \mathrm{i}\int_0^{\hat{L}} G(\mathbf{x},\mathbf{x}_0)\frac{\partial}{\partial \hat{y}}(G(\mathbf{x},\mathbf{x}_{src}) - G(\mathbf{x},\mathbf{x}_{snk}))\mathrm{d}\,\hat{x} \tag{50}$$

and

$$\frac{1}{2}\widehat{\mathscr{F}}(x_0,\omega)\zeta(x_0) + \fint_0^{\hat{L}} \hat{\mathscr{F}}(x,\omega)\zeta(x)\frac{\partial G(\mathbf{x},\mathbf{x}_0)}{\partial \hat{y}}\,\mathrm{d}\hat{x} + \hat{P}'(x_0) = 0, \tag{51}$$

where $\hat{x} = x/\mathscr{L}$, $\hat{y} = y/\mathscr{L}$, $\hat{L} = L/\mathscr{L}$, and $\mathscr{L}$ is a specified length scale. We have introduced the dimensionless membrane amplitude, pressure, and response function,

$$\zeta = \frac{F\mathscr{L}}{\varepsilon d}, \quad \hat{P}' \equiv \frac{P'}{\rho\omega^2\varepsilon d}, \quad \hat{\mathscr{F}} \equiv \frac{\mathscr{F}}{\rho\omega^2\mathscr{L}}. \tag{52}$$

### 4.1. Membrane at the channel centerline

Additional simplifications occur when the membrane is located at the center of the channel, $y_b = 0$, as the derivative of the Green's function inside the integral in (49) is zero, yielding

$$P'(x_0) = -\frac{1}{2}\mathscr{F}(x_0,\omega)F(x_0), \tag{53}$$

which merely expresses a pressure anti-symmetry condition. Substituting this expression in (48), we obtain an integral equation of the second kind for $F$ with a weakly singular (logarithmic) kernel,

$$\frac{1}{4}\mathscr{F}(x_0,\omega)F(x_0) = \rho\omega^2\int_0^L G(x,x_0)F(x)\,\mathrm{d}x - \mathrm{i}\omega\rho Q\int_0^L G(x,x_0)\frac{\partial}{\partial y}(G(\mathbf{x},\mathbf{x}_{src}) - G(\mathbf{x},\mathbf{x}_{snk}))\,\mathrm{d}x. \tag{54}$$

The associated dimensionless form is

$$\int_0^{\hat{L}} G(x,x_0)\zeta(\hat{x})\,\mathrm{d}\hat{x} - \frac{1}{4}\hat{\mathscr{F}}(x_0,\omega)\zeta(x_0) = \mathrm{i}\int_0^{\hat{L}} G(x,x_0)\frac{\partial}{\partial\hat{y}}(G(\mathbf{x},\mathbf{x}_{src}) - G(\mathbf{x},\mathbf{x}_{snk}))\,\mathrm{d}\hat{x}. \tag{55}$$

Evaluating (43) for $w_1 = -a, w_2 = a$, $w_3 = 0$, $h = 2a$, $y = 0$ and $y_0 = 0$, and simplifying, we find

$$G(x,x_0) = -\frac{1}{2\pi}\log\left|\sinh\frac{\pi(x-x_0)}{2a}\sinh\frac{\pi(x+x_0)}{2a}\right|. \tag{56}$$

For $x \sim a$ and $x_0 \gg a$, we obtain

$$G(x,x_0) \simeq \frac{1}{\pi}\log 2 - \frac{x_0}{2a}, \tag{57}$$

and thus

$$\int_0^{L} G(x,x_0)\frac{\partial}{\partial y}(G(\mathbf{x},\mathbf{x}_{src}) - G(\mathbf{x},\mathbf{x}_{snk}))\,\mathrm{d}x \simeq \frac{1}{\pi}\log 2 - \frac{x_0}{2a}, \tag{58}$$

which shows that the right-hand side of the integral equation grows linearly in $x_0$.

It is reassuring to confirm that the integral formulations remain unchanged when the Green's function is shifted by an arbitrary constant. Referring to (48), we find that this requires

$$\rho\omega^2\int_0^{L} F(x)\,\mathrm{d}x = \mathrm{i}\omega\rho Q\int_0^{L}\frac{\partial}{\partial y}(G(\mathbf{x},\mathbf{x}_{src}) - G(\mathbf{x},\mathbf{x}_{snk}))\,\mathrm{d}x. \tag{59}$$

The integral on the right-hand side is equal to unity, yielding

$$\int_0^{L} F(x)\,\mathrm{d}x = \mathrm{i}\frac{Q}{\omega} \quad \text{or} \quad \int_0^{L}\zeta(x)\,\mathrm{d}\hat{x} = \mathrm{i}, \tag{60}$$

in agreement with (22). This identity confirms the consistency of the boundary-integral formulation.

### 4.2. Hypersingular formulation

In an alternative approach, we take the derivative of the general equation (45) with respect to $y_0$, finding

$$\frac{\partial P'}{\partial y_0}(\mathbf{x}_0) = \int_0^{L}[P'](x)\frac{\partial^2 G(\mathbf{x},\mathbf{x}_0)}{\partial y\partial y_0}\,\mathrm{d}x. \tag{61}$$

Now we take the limit as $\mathbf{x}_0$ tends to the basilar membrane and substitute the kinematic and dynamic boundary conditions (34) and (35) to derive a hypersingular integral equation for the shape function, $F$,

$$\mathcal{H}\!\!\!\!\!\!\int_0^{L}\mathscr{F}(x,\omega)F(x)\frac{\partial^2 G(\mathbf{x},\mathbf{x}_0)}{\partial y\partial y_0}\,\mathrm{d}x + \rho\omega^2 F(x_0) = \mathrm{i}\rho\omega Q\frac{\partial}{\partial y}(G(\mathbf{x}_0,\mathbf{x}_{src}) - G(\mathbf{x}_0,\mathbf{x}_{snk})), \tag{62}$$

where $\mathscr{H}$ denotes the Hadamard or finite value part of the singular integral, properly defined in terms of the aforementioned limit. The associated dimensionless form is

$$\mathcal{H}\!\!\!\!\!\!\int_0^{\hat{L}}\hat{\mathscr{F}}(x,\omega)\zeta(x)\frac{\partial^2 G(\mathbf{x},\mathbf{x}_0)}{\partial\hat{y}\partial\hat{y}_0}\,\mathrm{d}\hat{x} + \zeta(x_0) = \mathrm{i}\frac{\partial}{\partial\hat{y}}(G(\mathbf{x}_0,\mathbf{x}_{src}) - G(\mathbf{x}_0,\mathbf{x}_{snk})). \tag{63}$$

This equation applies independent of the position of the basilar membrane between the upper and lower walls.

The term "hypersingular" describes the apparent $1/r^2$ singularity of the kernel of the integral equation, arising by twice differentiating the logarithmic Green's function. As $y_0 \to 0$, the kernel of the integral equation reduces to that of the free-space Green's function,

$$\frac{\partial^2 G(\mathbf{x},\mathbf{x}_0)}{\partial\hat{y}\partial\hat{y}_0} \simeq \mathscr{Y}(x,x_0,y_0) \equiv \frac{1}{2\pi}\frac{(x-x_0)^2 - y_0^2}{[(x-x_0)^2 + y_0^2]^2}. \tag{64}$$

Naively setting $y_0 = 0$ yields an intractable integral with respect to $x$. Instead, we perform the integration with respect to $x$ and then take the limit $y_0 \to 0$. To demonstrate the process, we compute the definite integral

$$\mathscr{I} = \int_{x_0-A}^{x_0+B} \mathscr{Y}(x, x_0, y_0)\,\mathrm{d}x = \frac{1}{2\pi y_0} \int_{-A/y_0}^{B/y_0} \frac{\omega^2 - 1}{(1+\omega^2)^2}\,\mathrm{d}\omega = -\frac{1}{2\pi y_0}\left[\frac{\omega}{1+\omega^2}\right]_{-A/y_0}^{B/y_0}. \tag{65}$$

Now taking the limit $y_0 \to 0$, we derive the finite part

$$\mathscr{I} = -\frac{1}{2\pi}\left(\frac{1}{B} + \frac{1}{A}\right). \tag{66}$$

To compute the integral of the hypersingular integral of a general Green's function, we remove the singularity by writing

$$\int_{x_0-A}^{x_0+B} \frac{\partial^2 G(\mathbf{x}, \mathbf{x}_0)}{\partial\hat{y}\partial\hat{y}_0}\,\mathrm{d}x = \int_{x_0-A}^{x_0+B} \left(\frac{\partial^2 G(\mathbf{x}, \mathbf{x}_0)}{\partial\hat{y}\partial\hat{y}_0} - \frac{1}{2\pi(x-x_0)^2}\right)\mathrm{d}x - \frac{1}{2\pi}\left(\frac{1}{B} + \frac{1}{A}\right). \tag{67}$$

The first integral on the right-hand side is nonsingular and can be computed by standard numerical methods.

## 5. Serial cochlear model

Lesser and Berkley (1972) proposed a serial rectangular cochlear model bounded by the stapes footplate located at $x = 0$, the round window located at $x = 2L$, the basilar membrane located at $y = 0$, and the cochlear wall located at $y = a$, as shown in Fig. 5(a). The boundary conditions specify a uniform velocity $V = \omega\varepsilon$ across the vertical inlet and outlet surfaces located at $x = 0$ and $2L$, yielding the flow rate $Q = Va = \omega\varepsilon a$. The pressure is assumed to be zero at the helicotrema located at $x = L$, and the membrane displacement is assumed to be anti-symmetric with respect to $x = L$. Fig. 5(b) explains that, in fact, the serial model emulates a fictitious anti-symmetric arrangement by ensuring that the membrane amplitude is zero at the helicotrema.

Allen (1977) developed a boundary-integral formulation using a Green's function that satisfies the no-penetration boundary condition at the horizontal planes $y = 0$, $y = a$, and at the vertical plane $x = 0$, and takes the value of zero over the mid-plane located at $x = L$. To derive this Green's function in a broader framework, we consider the potential $\Phi$ due to a point sink of unit strength located at an arbitrary point $\mathbf{x}_0$ and a point source of unit strength located at another arbitrary point $\mathbf{x}_1$, both placed inside a rectangular domain bounded by four walls located at $x = w_1$,

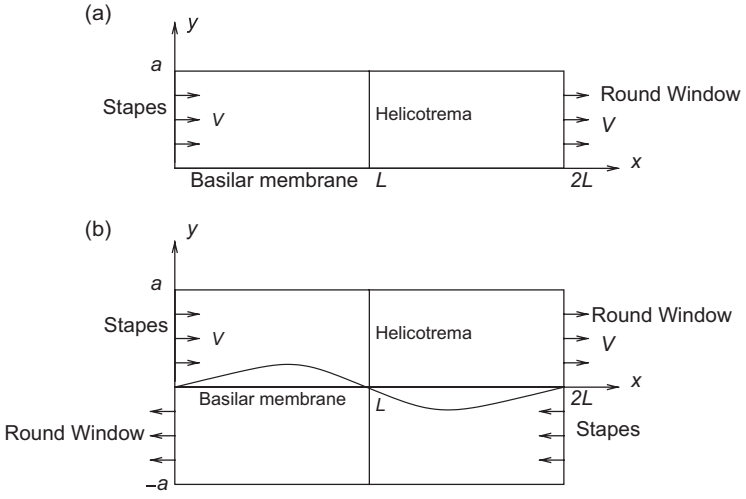


Fig. 5. (a) Illustration of the serial cochlea model where the scala tympani is unfolded and placed next to the scala vestibuli. (b) The serial model emulates an anti-symmetric arrangement by ensuring that the membrane amplitude is zero at the helicotrema.

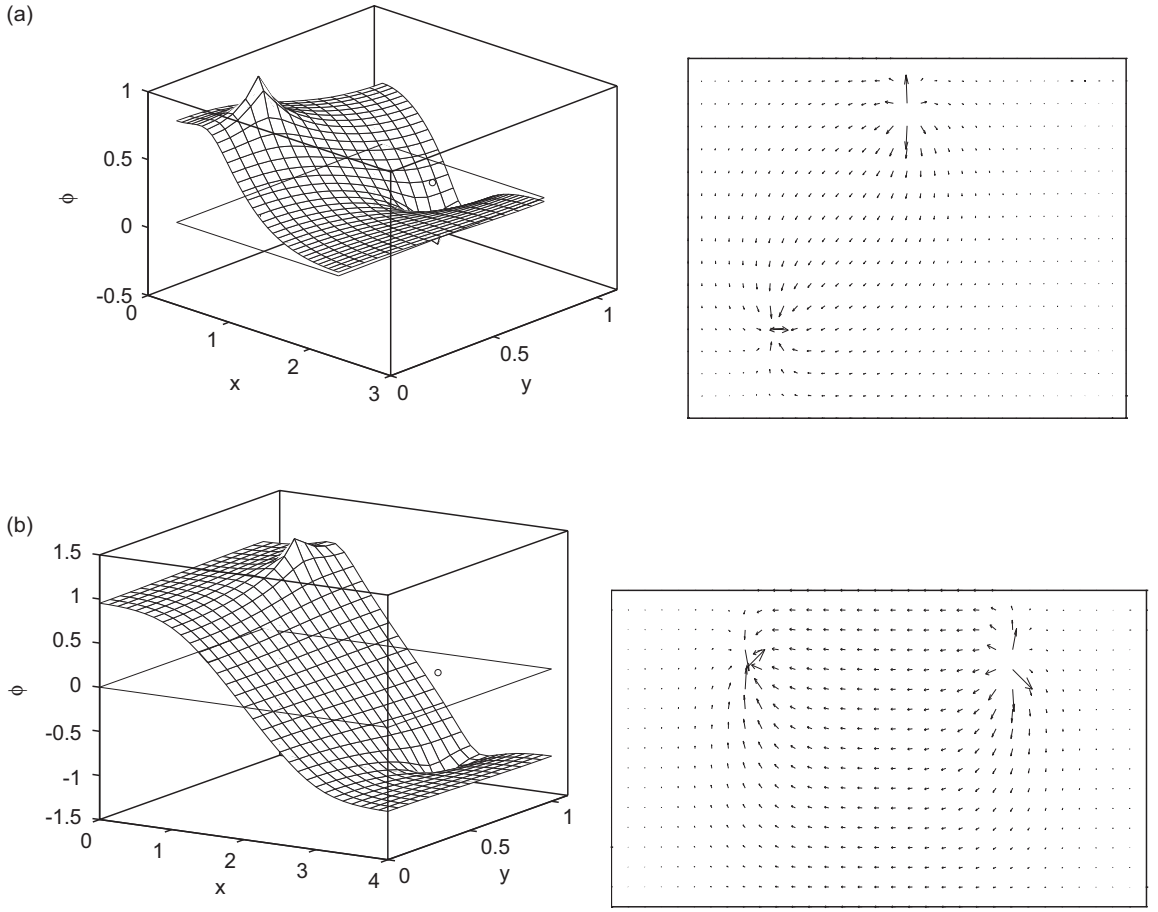


Fig. 6. (a) Potential and associated velocity vector field due to a point sink and a point source in a rectangular domain enclosed by four walls. (b) Green's function and associated gradient field of the serial cochlear model.

$x = w_2 > w_1$, $y = w_3$, and $y = w_4 > w_3$. Using the method of images, we find

$$\Phi_{w_1,w_2,w_3,w_4}(\mathbf{x},\mathbf{x}_0,\mathbf{x}_1) = \frac{x-(w_3+w_4)/2}{h} + \sum_{p=-\infty}^{\infty} [G_{w_1,w_2,w_3+2pw}(\mathbf{x},\mathbf{x}_0+2pw\mathbf{e}_x) - G_{w_1,w_2,w_4+2pw}(\mathbf{x},\mathbf{x}_1+2pw\mathbf{e}_x)], \tag{68}$$

where $h = w_2 - w_1$, $w = w_4 - w_3$, $\mathbf{e}_x$ is the unit vector along the $x$ axis, and the strip Green's function $G$ is given in (43). A graph of this potential and corresponding velocity vector field for a sample configuration is shown in Fig. 6(a).

The Green's function of the cochlear model adopted by Allen (1977) arises by setting $w_1 = 0$, $w_2 = a$, $w_3 = 0$, and $w_4 = 2L$, yielding $h = a$, $w = 2L$, and

$$\mathscr{G}(\mathbf{x},\mathbf{x}_0) = \Phi_{0,a,0,2L}(\mathbf{x},\mathbf{x}_0,\mathbf{x}_0^R), \tag{69}$$

where $\mathbf{x}_0^R = (2L - x_0, y_0)$ is the reflection of the singular point $\mathbf{x}_0$ with respect to the helicotrema. Explicitly,

$$\mathscr{G}(\mathbf{x},\mathbf{x}_0) = \frac{x-L}{a} + \sum_{p=-\infty}^{\infty} [G_{0,a,4pL}(\mathbf{x},\mathbf{x}_0+4pL\mathbf{e}_x) - G_{0,a,2L+4pL}(\mathbf{x},\mathbf{x}_0^R+4pL\mathbf{e}_x)]. \tag{70}$$

A graph of this Green's function and corresponding gradient field for a sample location of the singular point is shown in Fig. 6(b). For the large aspect ratio $L/a$ of present interest, retaining only one term in the sum corresponding to $p = 0$ is sufficient for achieving accuracy up to the sixth decimal.

Now applying Green's third identity for the flow in the left compartment of Fig. 5(a) and implementing the kinematic condition $\partial P/\partial y = \rho\omega^2 F$ along the membrane and the kinematic condition $\partial P/\partial x = -\mathrm{i}\rho\omega V$ along the stapes footplate, we derive the counterpart of the integral representation (48) for the total pressure amplitude,

$$P(\mathbf{x}_0) = -\rho\omega^2 \int_0^L \mathscr{G}(\mathbf{x}, \mathbf{x}_0) F(x)\, \mathrm{d}x + \mathrm{i}\rho\omega V \int_0^a \mathscr{G}(\mathbf{x}, \mathbf{x}_0)\, \mathrm{d}y. \tag{71}$$

The first integral is computed along the basilar membrane located at $y = 0$, and the second integral is computed along the stapes located at $x = 0$. A missing factor of two in Allen's (1977) formulation is noted in Allen and Sondhi (1979, footnote 2). The second integral in (71) represents the potential due to a uniform distribution of point sinks along the stapes, complemented by a uniform distribution of point sources along the oval window, and is thus equal to $L - x_0$ independent of $a$. Moving the field point $\mathbf{x}_0$ to the basilar membrane, setting $V = \omega\varepsilon$, $P(x_0, \omega) = \frac{1}{2}[P](x_0) = -\frac{1}{2}\mathscr{F} F$, and rearranging, we derive the integral equation

$$\frac{1}{2}\mathscr{F}(x_0, \omega) F(x_0) = \rho\omega^2 \int_0^L \mathscr{G}(x, x_0) F(x)\, \mathrm{d}x - \mathrm{i}\rho\omega^2 \varepsilon a \frac{L - x_0}{a}. \tag{72}$$

The dimensionless form of (72) is the counterpart of (55),

$$\int_0^{\hat{L}} \mathscr{G}(x, x_0)\zeta(\hat{x})\, \mathrm{d}\hat{x} - \frac{1}{2}\hat{\mathscr{F}}(x_0, \omega)\zeta(x_0) = \mathrm{i}\frac{\hat{L} - \hat{x}_0}{\hat{a}}, \tag{73}$$

where $\hat{L} = L/\mathscr{L}$, $\hat{a} = a/\mathscr{L}$, and the stapes footplate length in the definition of $\zeta$ has been set to $d = a$. To explain the different factors $\frac{1}{2}$ and $\frac{1}{4}$ in front of the second terms on the left-hand sides of (73) and (55), we note that, as $x \to x_0$, $G$ tends to $-(1/2\pi)\ln|x - x_0|$, whereas $\mathscr{G}$ tends to $-(1/\pi)\ln|x - x_0|$ due to presence of an image system across the basilar membrane.

To be more specific, we truncate the sum in (70) after one term corresponding to $p = 0$, and substitute (43) to find

$$\mathscr{G}(x, x_0) \simeq \frac{x - L}{a} + 2G(x, x_0) + \frac{1}{\pi}\log\left|\sinh\frac{\pi(2L - x + x_0)}{2a} \times \sinh\frac{\pi(2L - x - x_0)}{2a}\right|, \tag{74}$$

where $G(x, x_0)$ is given in (56). Far from the helicotrema, $2L - x + x_0 \gg 0$, and $2L - x - x_0 \gg 0$, this expression simplifies to

$$\mathscr{G}(x, x_0) \simeq 2G(x, x_0) + \frac{L}{a} - \frac{2}{\pi}\log 2. \tag{75}$$

Solving for $G(x, x_0)$, substituting in (55), and using (60), we find

$$\int_0^{\hat{L}} \mathscr{G}(x, x_0)\zeta(\hat{x})\, \mathrm{d}\hat{x} - \frac{1}{2}\hat{\mathscr{F}}(x_0, \omega)\zeta(x_0) = \mathrm{i}\left[\frac{L}{a} - \frac{2}{\pi}\log 2 + 2\int_0^{\hat{L}} G(x, x_0)\frac{\partial}{\partial\hat{y}}(G(\mathbf{x}, \mathbf{x}_{src}) - G(\mathbf{x}, \mathbf{x}_{snk}))\, \mathrm{d}\hat{x}\right]. \tag{76}$$

Eq. (58) shows that the ratio of the right-hand sides of (73) and (76) tends to unity far from the stapes and far from the helicotrema, yielding similar solutions.

In summary, the key features of the serial cochlea model are that the oval and round window move with a uniform velocity across the cochlea partitions, and the basilar membrane displacement is zero at the helicotrema.

## 6. Consistent rectangular cochlear model

In the most complete formulation, we allow for the presence of the helicotrema and regard the scala vestibuli and scala tympani as a contiguous medium. The pressure field is reconstructed in terms of the potential $\Phi$ defined in (68), yielding the counterpart of (31),

$$P = \mathrm{i}\omega\rho Q \Phi_{w_1, w_2, w_3, w_4}(\mathbf{x}, \mathbf{x}_{src}, \mathbf{x}_{snk}) + P'. \tag{77}$$

For simplicity, heretoforth we omit the subscripts $w_1 - w_4$. Next, we choose two points $\mathbf{x}_0$ and $\mathbf{x}_1$ inside the scala vestibuli or scala tympani, and apply Green's third identity to obtain the counterpart of (45),

$$P'(\mathbf{x}_0) = P'(\mathbf{x}_1) + \int_0^L [P'](x)\frac{\partial\Phi(\mathbf{x}, \mathbf{x}_0, \mathbf{x}_1)}{\partial y}\, \mathrm{d}x, \tag{78}$$

where the integral is computed along the length of the basilar membrane. Taking the derivative of (78) with respect to $y_0$ while holding $\mathbf{x}_1$ constant, we find

$$\frac{\partial P'}{\partial y_0}(\mathbf{x}_0) = \int_0^L [P'](x) \frac{\partial^2 \Phi(\mathbf{x}, \mathbf{x}_0, \mathbf{x}_1)}{\partial y \partial y_0} \, \mathrm{d}x. \tag{79}$$

Now we take the limit as $\mathbf{x}_0$ tends to $B$ and substitute the kinematic and dynamic boundary conditions (34) and (35) to derive a hypersingular integral equation for the shape function, $F$,

$$\mathcal{H}\!\!\!\!\!\!\int_0^L \mathscr{F}(x,\omega) F(x) \frac{\partial^2 \Phi(\mathbf{x}, \mathbf{x}_0, \mathbf{x}_1)}{\partial y \partial y_0} \, \mathrm{d}x + \rho \omega^2 F(x_0) = \mathrm{i} \rho \omega Q \Phi(\mathbf{x}, \mathbf{x}_{src}, \mathbf{x}_{snk}). \tag{80}$$

The associated dimensionless form is

$$\mathcal{H}\!\!\!\!\!\!\int_0^{\hat{L}} \hat{\mathscr{F}}(x,\omega) \zeta(x) \frac{\partial^2 \Phi(\mathbf{x}, \mathbf{x}_0, \mathbf{x}_1)}{\partial \hat{y} \partial \hat{y}_0} \, \mathrm{d}\hat{x} + \rho \omega^2 \zeta(x_0) = \mathrm{i} \Phi(\mathbf{x}, \mathbf{x}_{src}, \mathbf{x}_{snk}). \tag{81}$$

This formulation is attractive in that the integral equation (81) applies independently of the position of the basilar membrane. In practice, the evaluation of the hypersingular integral fails at the end of the solution domain due to the singular nature of potential flow around a flat plate. A more sophisticated analysis that incorporates the presence of Stokes boundary layers is necessary.

## 7. Numerical methods

The solution of the integral equations for the rectangular models discussed in previous sections was found by dividing the solution domain, $0<x<L$, into $N$ evenly spaced segments, and applying point collocation at the segment mid-points, $\mathbf{x}_i^M$, where $i = 1, \ldots, N$.

The discretized integral equations (50) and (51) for the semi-infinite cochlear model read

$$\sum_{j=1}^N A_{ij} \zeta_j + \sum_{j=1}^N \left( \frac{1}{2} \delta_{ij} - B_{ij} \right) \hat{P}_j' = \mathrm{i} \sum_{j=1}^N A_{ij} (G(\mathbf{x}_j^M, \mathbf{x}_{src}) - G(\mathbf{x}_j^M, \mathbf{x}_{snk})) \tag{82}$$

and

$$\sum_{j=1}^N \left( \frac{1}{2} \delta_{ij} + B_{ij} \right) \hat{\mathscr{F}}_j \zeta_j + \hat{P}_i' = 0, \tag{83}$$

for $i = 1, \ldots, N$, where $\zeta_j$, $\hat{P}_j'$, and $\hat{\mathscr{F}}_j$ are the dimensionless membrane amplitude, upper surface pressure, and response function at the center of the $j$th interval, $\delta_{ij}$ is Kronecker's delta, and we have defined the influence coefficients

$$A_{ij} = \int_{x_j}^{x_{j+1}} G(\mathbf{x}, \mathbf{x}_i^M) \, \mathrm{d}\hat{x}, \quad B_{ij} = \mathcal{P}\!\!\!\!\!\!\int_{x_j}^{x_{j+1}} \frac{\partial G(\mathbf{x}, \mathbf{x}_i^M)}{\partial y} \, \mathrm{d}x. \tag{84}$$

The integrals in (84) are computed using the six-point Gauss–Legendre quadrature. The logarithmic singularity exhibited by the Green's function is subtracted off and integrated analytically over the singular elements. Because the solution domain is a straight line, a singularity does not appear in the kernel of the principal value of the double-layer integral, $B_{ij}$. The algebraic equations (82) and (83) are compiled in a linear system, where the unknown solution vector contains the element values, $\zeta_j$ and $\hat{P}_j'$.

The discretized integral equation (55) for the semi-infinite model with the membrane located mid-way between the upper and lower walls reads

$$\sum_{j=1}^N \left( A_{ij} - \frac{1}{4} \hat{\mathscr{F}}(x_i^M, \omega) \delta_{ij} \right) \zeta_j = \mathrm{i} \sum_{j=1}^N A_{ij} (G(\mathbf{x}_j^M, \mathbf{x}_{src}) - G(\mathbf{x}_j^M, \mathbf{x}_{snk})), \tag{85}$$

for $i = 1, \ldots, N$, yielding a linear system for the element values, $\zeta_j$.

The weakly singular integral equation of the serial cochlear model is treated by similar methods. To solve the hypersingular integral equation (62), we evaluate the hypersingular integrals over the straight segments using the method discussed at the end of Section 4.2.

The solution of the derived complex linear systems of equations was found by the method of LU decomposition embedded in Matlab. The computational cost for each case study is a few minutes of CPU time on a personal computer. As long as the computed wave packet is far from the helicotrema, results based on the formulation with the weakly singular integral equations are in excellent agreement with those based on the formulation with the hypersingular integral equation. When the wave packet reaches the helicotrema, the hypersingular formulation exhibits a slow convergence with respect to the number of boundary elements due to strong end-effects. Unless stated otherwise, all results presented in the remainder of this paper are based on the weakly singular formulation with the semi-infinite model. The accuracy will be demonstrated in the next section by case-study solutions.

## 8. Frequency-domain response

In this section, we discuss the membrane response in the frequency domain for different membrane response functions, compare the results with previous analytical and numerical solutions, and perform parametric investigations to demonstrate the effect of the various system parameters.

### 8.1. Inertialess membrane

We begin by considering the oscillations of the membrane subject to the membrane response function

$$\mathscr{F}(x,\omega) = s_0 \mathrm{e}^{-\lambda(x-x_r)}(1+\mathrm{i}\omega\beta), \tag{86}$$

and set the characteristic length equal to the channel width, $\mathscr{L} = h = 2a$. The solution of the integral equations derived in the previous sections depends on four dimensionless parameters,

$$\hat{s}_0 \equiv \frac{s_0\beta^2}{\rho h}, \quad \frac{x_r}{h}, \quad \lambda h, \quad \omega\beta. \tag{87}$$

When $\hat{s}_0 = 0$, the basilar membrane is a passive material surface oscillating under the influence of the flow generated by the point source and point sink. The motion describes a standing wave whose peak amplitude is near these singularities. As the value of $\hat{s}_0$ is raised, the membrane elastic properties become increasingly important, the membrane vibration describes a traveling wave, and the peak amplitude of the wave envelop moves farther into the cochlea.

Fig. 7(a–d) shows numerical solutions for $\hat{s}_0 = 2.5\times10^{-8}$ and $\lambda h = \frac{4}{7}$, computed with the semi-infinite cochlear model for $x_r/h = 30$, domain truncation level $x/h = 20$, and $N = 256$ intervals. The point source is located at $x_{src} = 0.01h$, $y_{src} = 0.25h$, the point sink is located at $x_{src} = 0.01h$, $y_{src} = -0.25h$, and the basilar membrane is located at the channel centerline, $y_b = 0$. The solution describes a wave packet consisting of a sinusoidal wave whose wave length decreases exponentially with downstream position, $x$. As the dimensionless frequency $\beta$ is raised, the peak of the wave packet is shifted toward the beginning of the basilar membrane, and the number of waves contained in the envelop becomes smaller. Fig. 7(e, f) confirms that the predictions of the hypersingular formulation are in excellent agreement with those of the weakly singular formulation.

Fig. 7(g, h) shows the predictions of the serial cochlea model discussed in Section 5. Even though the driving mechanism is attributed to a piston-like motion of the stapes and round window, the results are remarkably similar to those of the point source model. This comparison underscores the insignificance of the precise location of the source driving the fluid motion after a periodic state has been established. In Section 9, we shall see that this not necessarily the case for a more general time-dependent response.

Fig. 8 illustrates the convergence of the numerical solution with respect to the number of intervals for the most demanding low-frequency computation, $\omega\beta = 0.05$, and for a medium-frequency computation, $\omega\beta = 0.20$. In the first case, increasing the number of intervals captures a higher number of waves at the downstream side of the envelop, but has a small effect on the upstream side of the wave. In the second case, the computation with $N = 128$ intervals is able to capture with good accuracy the whole waveform. Changing the parameter $x_r$ causes a mere shift in the location of the peak without drastically altering the overall wave form, as shown in Fig. 9 for $\omega\beta = 0.5$ and $x_r/h = 35$ or 40.

LeVeque et al. (1985) considered the vibration of the basilar membrane far from the stapes and round window in an infinite domain extending over $-\infty < x < \infty$, under assumptions similar to those adopted in the present model.

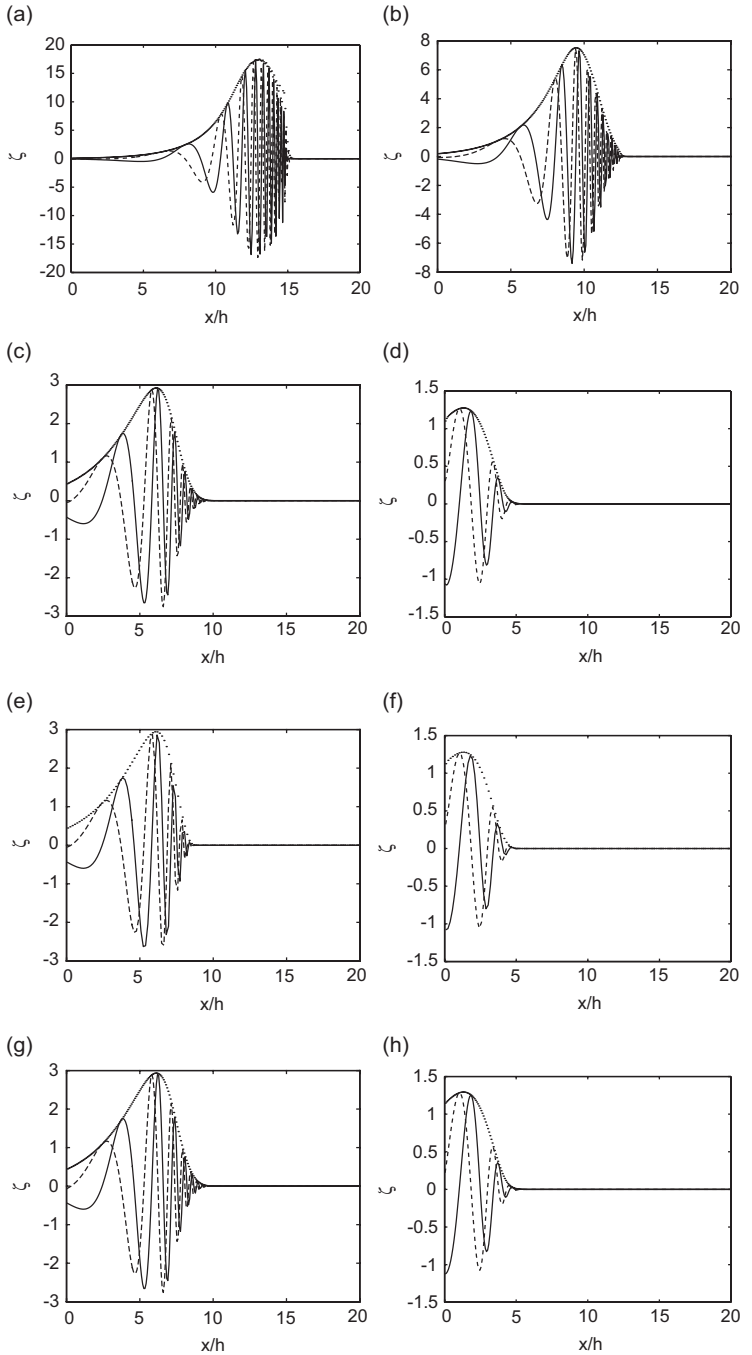


Fig. 7. Real part (solid lines), imaginary part (dashed lines), and magnitude (dotted lines) of the membrane vibration amplitude for $\hat{s}_0 = 2.5 \times 10^{-8}$, $\lambda h = 4/7$, $x_r/h = 30$, and (a–d) $\omega\beta = 0.05$, 0.1, 0.2, and 0.5. (e, f) Corresponding results with the hypersingular formulation for $\omega\beta = 0.2$ and 0.5. (g, h) Corresponding results with the serial cochlear model for $\omega\beta = 0.2$ and 0.5.

Their analysis demonstrated that the Fourier transform of the basilar membrane amplitude function,

$$\hat{F}(\xi) \equiv \int_{-\infty}^{\infty} F(x)\, \mathrm{e}^{-2\pi \mathrm{i}\xi x}\, \mathrm{d}x, \tag{88}$$

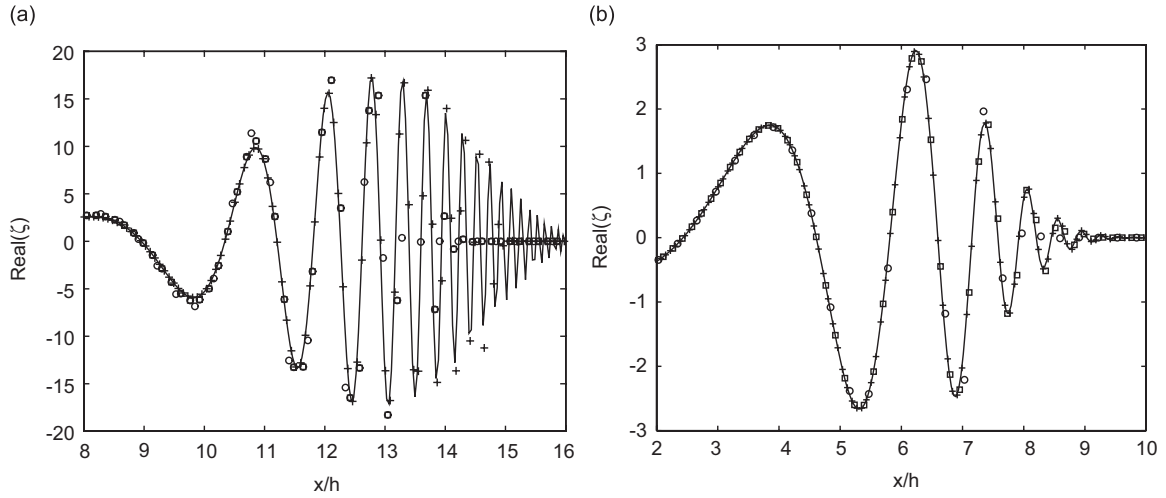


Fig. 8. Convergence of the numerical solution with respect to the number of intervals for $\hat{s}_0 = 2.5 \times 10^{-8}$, $\lambda h = 4/7$, $x_r/h = 30$, and (a) $\omega\beta = 0.05$ or (b) 0.20. The circles, squares, crosses, and solid line correspond, respectively, to $N = 64$, 128, 256, and 512.

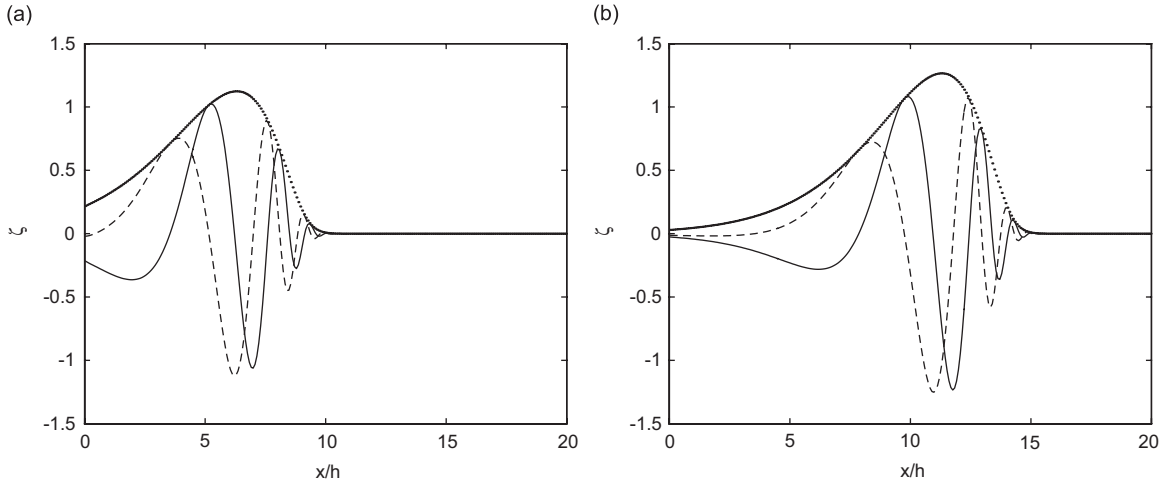


Fig. 9. Real part (solid lines), imaginary part (dashed lines), and magnitude (dotted lines) of the membrane vibration amplitude for $\hat{s}_0 = 2.5 \times 10^{-8}$, $\lambda h = 4/7$, $\omega\beta = 0.5$, and (a) $x_r/h = 35$ or (b) 40.

satisfies the functional equation

$$\hat{F}(\xi) = \hat{K}(\xi)\hat{F}\left(\xi - \frac{\lambda \mathrm{i}}{2\pi}\right), \tag{89}$$

where $\hat{K}(\xi) \equiv \alpha\xi \tanh(2\pi a\xi)$ and $\alpha = (\pi s_0)/(\rho\omega^2)(1 + \mathrm{i}\omega\beta)$. As the channel semi-width $a$ tends to infinity, $\hat{K}(\xi) \to \alpha|\xi|$. By numerically inverting the Fourier transform, the authors displayed numerical results for $\hat{s}_0 = 2.5 \times 10^{-8}$, $\lambda h = \frac{4}{7}$, and three reduced frequencies $\omega\beta = 0.05$, 0.1, and 0.2. Moreover, the authors provided asymptotic estimates for the location of the peak and rates of the decay far from the peak.

The graphs shown in Fig. 7(a–c) are remarkably similar to those shown in the second column of Fig. 1 of LeVeque et al. (1985). We find that the amplitude of the wave peaks at approximately $x_p/h \simeq 13$, 9, and 6, respectively, for $\omega\beta = 0.05$, 0.01, and 0.2, corresponding to $\lambda(x_p - x_r) = (\frac{4}{7})(x_p - x_r)/h \simeq -9.7$, $-12.0$, and $-13.7$. LeVeque et al. (1985) in their Table 1 cite values that can be transformed to yield $\lambda(x_p - x_r) = -9.8$, $-11.7$, and $-13.6$. These are in excellent

agreement with the present numerical results, even though our model explicitly accounts for the presence of a point source and a point sink. To explain this remarkable agreement, we recast the integral equation (54) into the form

$$\frac{1}{4}s_0(1+\mathrm{i}\omega\beta)\,\mathrm{e}^{-\lambda x_0}F(x_0)=\omega^2\rho\int_{-\infty}^{\infty}G(x-x_0)F_1(x)\,\mathrm{d}x, \tag{90}$$

where

$$F_1(x)=F(x)-\frac{\mathrm{i}Q}{\omega}\frac{\partial}{\partial y}(G(\mathbf{x},\mathbf{x}_{src})-G(\mathbf{x},\mathbf{x}_{snk})); \tag{91}$$

the $x$ axis has been shifted so that $x_r=0$, and the domain of integration has been extended over the whole of the $x$ axis under the assumption that $F(x)$ decays rapidly far from the shifted origin. Taking the Fourier transform with respect to $x$ and using the convolution theorem, we find

$$\frac{1}{4}s_0(1+\mathrm{i}\omega\beta)F\left(\xi-\frac{\lambda\mathrm{i}}{2\pi}\right)=\omega^2\rho\hat{L}(\xi)\hat{F}_1(\xi), \tag{92}$$

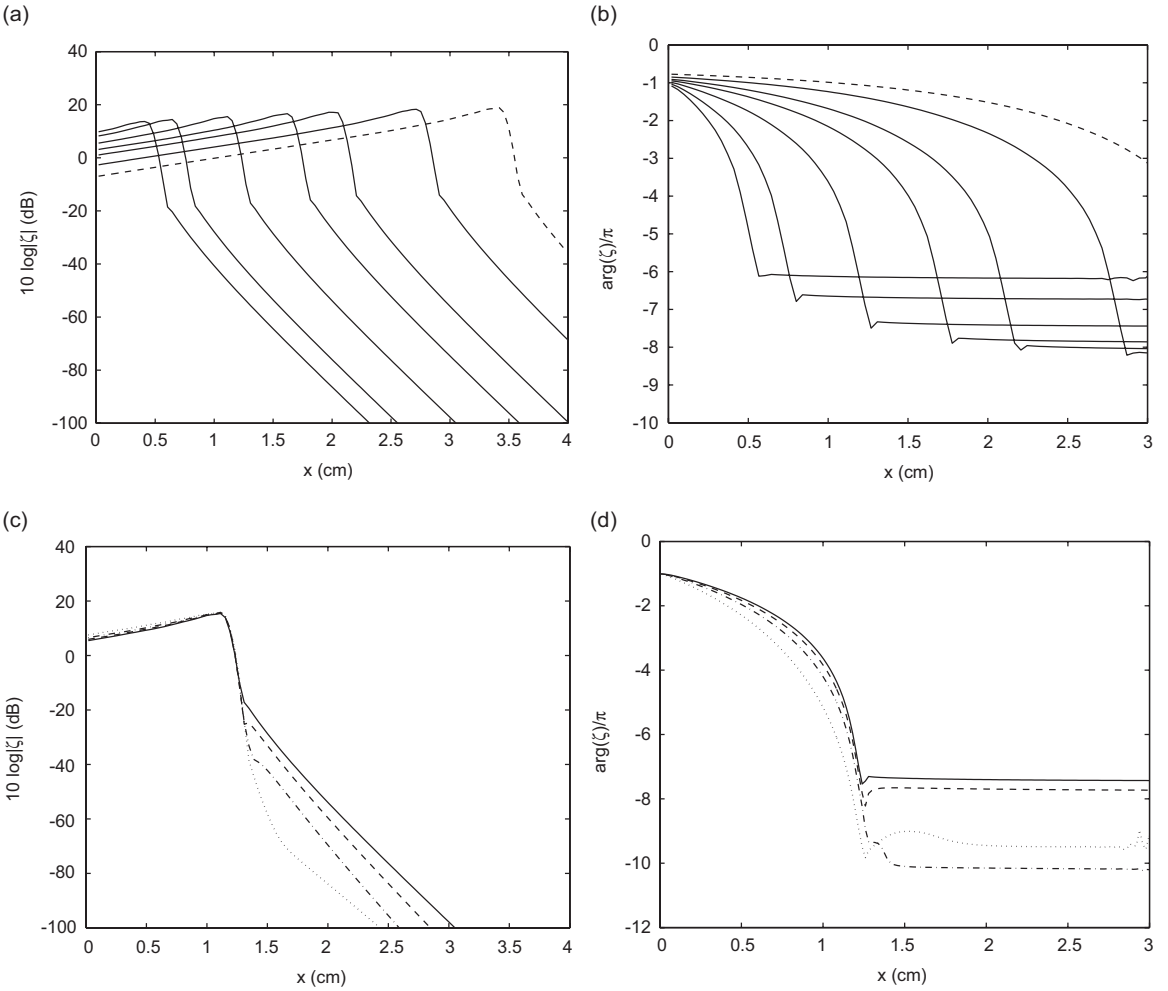


Fig. 10. (a) Amplitude of the traveling wave plotted against distance on a logarithmic scale, and (b) corresponding phase for frequencies $f=0.5$ (dashed line), 1, 2, 3, 5, 8, 10 kHz. (c, d) Effect of the basilar membrane position across the cochlear channel on (c) the amplitude, and (d) phase of the membrane vibration for $f=5$ kHz. The solid, dashed, dashed-dot, and dotted lines correspond, respectively, to $y_b=0$, 0.4, 0.6, and 0.8 cm.

where $\hat{L}(\xi)$ is the Fourier transform of the Green's function regarded as a tempered distribution (LeVeque et al., 1985). Neglecting as a first approximation the presence of the walls, we use the logarithmic kernel $G(x-x_0) \simeq -(1/2\pi)\log|x-x_0|$ and set $\hat{L}(\xi) = 1/(4\pi|\xi|)$ to obtain a functional equation that is identical to that shown in (89). To account for the presence of the upper and lower walls, we use the modified kernel $G(x-x_0) = -(1/2\pi)\log|\sinh \pi(x-x_0)/2a|$, and deduce that its inverse Fourier transform is given by $\hat{L}(\xi) = \alpha/(4\pi\hat{K}(\xi))$.

### 8.2. General membrane response

Next, we consider the more realistic membrane response function expressed by (29), refer to dimensional units in the CGI system, and adopt the physiological values

$$c = 1.72\times 10^9\, e^{-2x}\,\mathrm{dyn/cm^3}, \quad \kappa = 1.20\times 10^3\, e^{-x}\,\mathrm{dyn\,s/cm^3}, \quad m = 0.143\,\mathrm{g/cm^2}, \tag{93}$$

where the distance $x$ is measured in cm. Kagawa et al. (1987) found that these values yield the least disagreement with Rhode's (1971) laboratory data. The half-depth of the cochlear channel is $a = 0.1$ cm, and the density of the perilymph is taken to be equal to that of water, $\rho = 1\,\mathrm{g/cm^3}$. Fig. 10(a, b) shows the amplitude and phase of the membrane

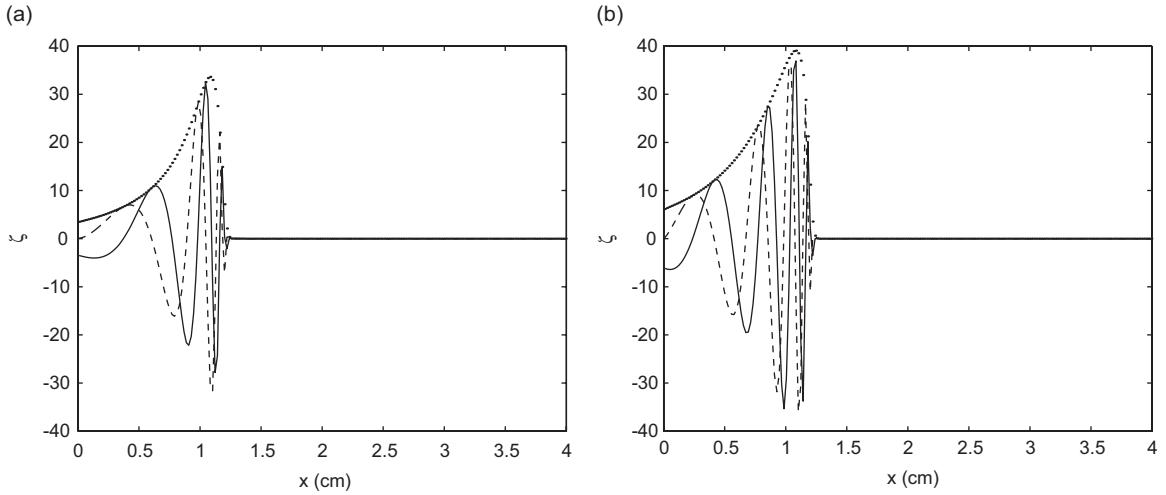


Fig. 11. Effect of basilar membrane position across the cochlear channel. Real (solid lines), imaginary (dashed lines), and magnitude (dotted lines) of the basilar membrane vibration amplitude for $f = 5$ kHz, and (a) $y_b = 0$, or (b) 0.08 cm.

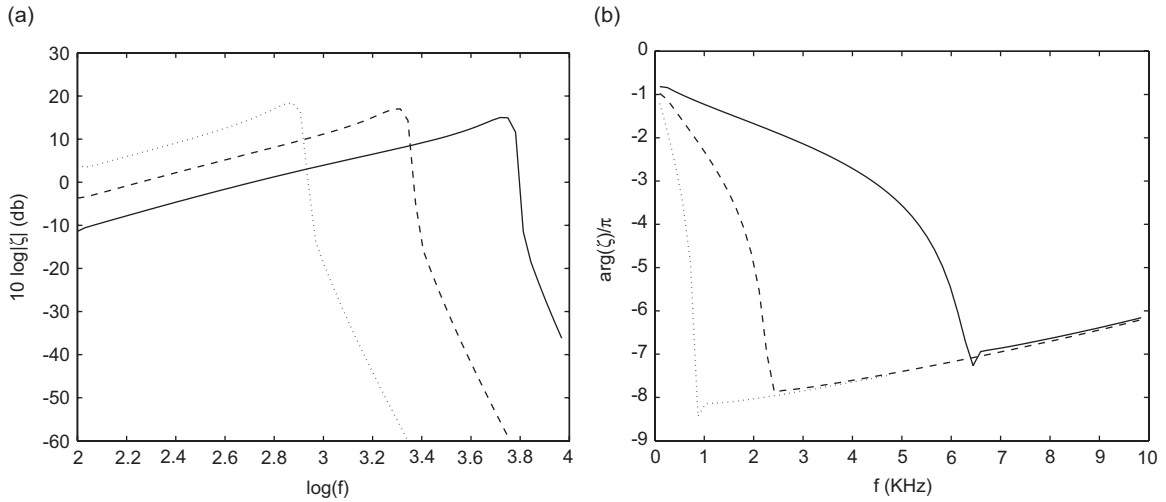


Fig. 12. Vibration amplitude and phase at three locations, $x = 1$, 2, and 3 cm, corresponding to the solid, dashed, and dotted lines.

vibration amplitude, $\zeta$, for frequencies $f = 0.5$ (dashed line), 1, 2, 3, 5, 8, and 10 kHz. The characteristic length $\mathscr{L}$ in the definition of $\zeta$ is set equal to 1 cm. The near-discontinuity in each curve marks the end of the envelop of the traveling wave. Note that the amplitude is plotted against distance on a semi-logarithmic scale and expressed in decibels. In this calculation, the point source is located at $x_{src} = 0.01$ cm, $y_{src} = 0.05$ cm, the point sink is located at $x_{snk} = 0.01$ cm, $y_{snk} = -0.05$ cm, and the basilar membrane is located at the channel centerline, $y_b = 0$.

The results are in qualitative agreement with those presented in Kagawa et al. (1987, Fig. 6) obtained by a finite element method that relies on a variational formulation to implement the action of the stapes and round window. In the model of Kagawa et al. (1987), the stapes and round window occupy the whole channel cross-section at the left wall, both vibrating with a uniform prescribed velocity. Quantitative differences between the present and previous results are observed at the end of the envelop of the traveling wave. Unfortunately, Kagawa et al. (1987) do not discuss the discretization level and accuracy of their finite element solutions.

Additional simulations have revealed that the predicted membrane oscillations depend only weakly on the assumed position of the point source and point sink, as well as on the lateral position of the membrane across the cochlear channel. Fig. 10(c, d) shows the effect of the basilar membrane position on the amplitude and phase of the vibration for

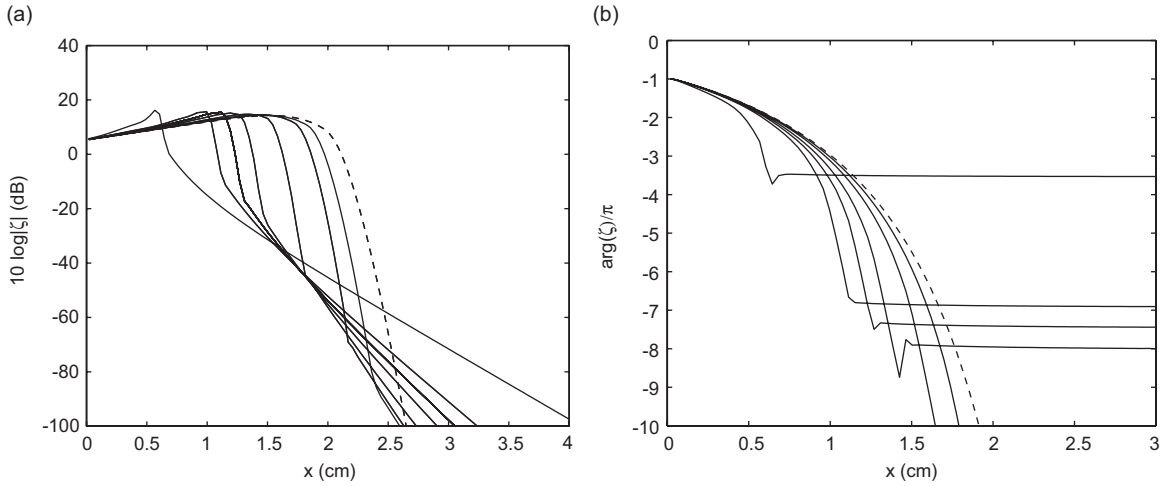


Fig. 13. Effect of membrane surface density on the (a) amplitude and (b) phase of the membrane wave at the frequency $f = 5$ kHz. The responses shown correspond to $m = 0$ (dashed line) 0.02, 0.05 0.10, 0.143, 0.20, and 0.5 g/cm$^2$.

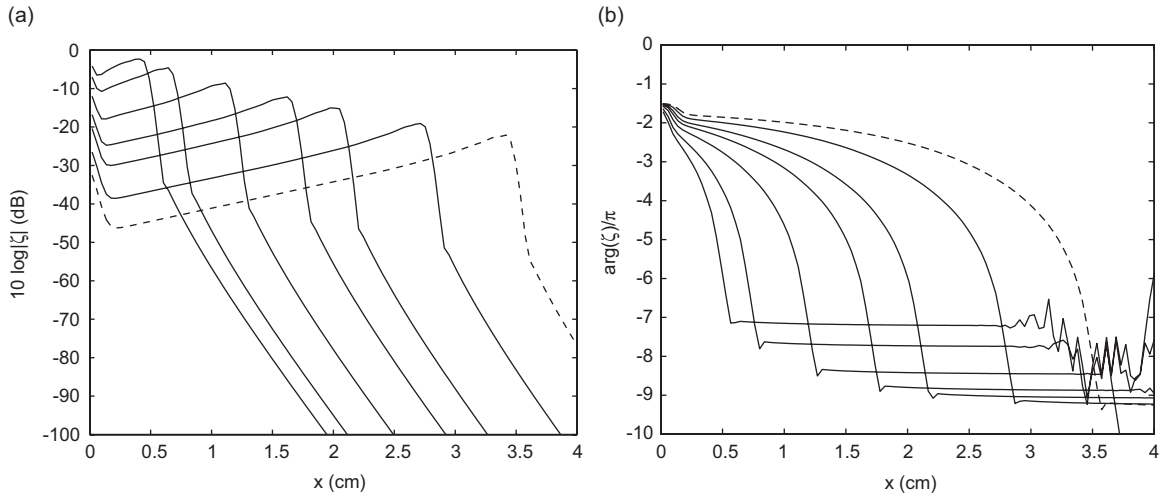


Fig. 14. Membrane vibrations induced by a dipole emulating the rocking motion of the stapes. (a) Amplitude of the traveling wave plotted against distance on a logarithmic scale, and (b) corresponding phase for frequencies $f = 0.5$ (dashed line), 1, 2, 3, 5, 8, and 10 kHz. Numerical noise arises in the high-frequency solution.

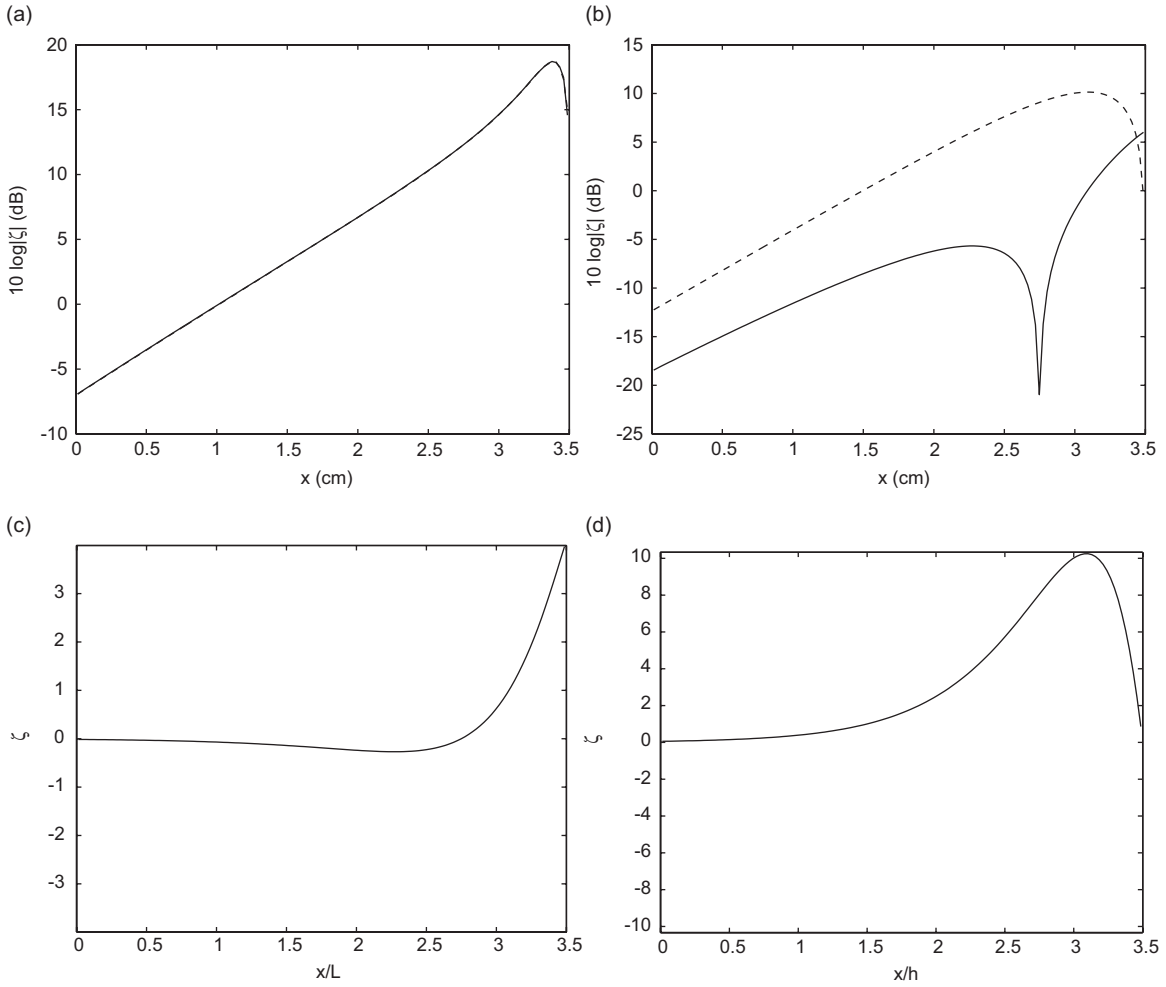


Fig. 15. Membrane vibration amplitude as predicted by the semi-infinite parallel cochlea model (solid line) and the serial cochlea model (dashed line), for frequencies (a) 500 Hz and (b) 100 Hz. Instantaneous wave forms at 100 Hz for the parallel and serial models are shown in (c) and (d).

frequency $f = 5\,\text{kHz}$. The point source is located at $x_{src} = 0.01\,\text{cm}$, $y_{src} = 0.09\,\text{cm}$, the point sink is located at $x_{snk} = 0.01\,\text{cm}$, $y_{snk} = -0.09\,\text{cm}$, and the basilar membrane is located at $y_b = 0$, 0.04, 0.06, and 0.08 cm. Comparing these graphs with the corresponding graphs for $f = 5\,\text{kHz}$ shown in Fig. 10(a, b) reveals the weak effect of the precise location of the singularities. Fig. 11 illustrates the structure of the traveling wave for $y_b = 0$ and 0.08 cm, where noticeable but not drastic differences can be identified.

Laboratory experiments have measured the vibration of a basilar membrane at a fixed location as a function of the vibration frequency (von Békésy, 1960; Rhode, 1971). Fig. 12 shows a graph of the vibration amplitude and phase predicted by the present boundary-integral formulation at three locations $x = 1$, 2, and 3 cm, plotted against the vibration frequency, for $y_b = 0$. A comparison with Rhode's data reported in Zweig et al. (1976, Fig. 4) reveals similar qualitative trends but noticeable quantitative differences in one of the two graphs. Similar discrepancies were noted by previous authors and attributed to a number of reasons, including the nonlinear response of the basilar membrane at the high excitation levels applied in the laboratory studies.

All results presented thus far were obtained using the Kagawa et al. (1987) value for the effective surface density of the basilar membrane system, $m = 0.143\,\text{g/cm}^2$. This effective density includes the mass of the endolymph contained between the vestibular and basilar membrane. To demonstrate the significance of the membrane mass, in Fig. 13 we present the membrane response at the frequency $f = 5\,\text{kHz}$ for a series of membrane densities, keeping the membrane stiffness, $c$, and viscous resistance coefficient, $\kappa$, constant. We see that, as the membrane density increases, the location

of the peak of the response curve is shifted toward the oval window, while the maximum amplitude remains nearly constant. Significant changes in the shape of the response curves are observed when the membrane inertia dominates. We conclude that the membrane mass is an important determinant of the basilar membrane vibration.

The stapes footplate may exhibit a rocking motion in a addition to the piston-like vibration. The effect of the rocking motion may be represented by a point source dipole superposed on the point source. In our model, we simply add a point sink with appropriate strength near the point source in the scala vestibuli. In one extreme case, we translate the point sink emulating the vibration of the round window. The cochlear response due to the resulting dipole is illustrated in Fig. 14. The rocking motion generates traveling waves whose peak amplitude is significantly smaller than that induced by the piston-like displacement.

Fig. 15 compares results obtained using the semi-infinite parallel cochlea model (solid lines) or the serial model (broken lines). The latter requires that the membrane vibration amplitude is zero at the helicotrema, whereas the former allows for a free motion. At the frequency $f = 500\,\text{Hz}$, the peak of the wave packet is located sufficiently far from the helicotrema, and the two models predict virtually identical behavior. Significant differences are observed at the lower frequency 100 Hz. The parallel model predicts a traveling wave whose amplitude reduces to zero at a node located at $x \simeq 2.75\,\text{cm}$. Another traveling wave is established thereafter, as illustrated in Fig. 15(c). These comparisons underscore the importance of the downstream boundary condition in the low-frequency acoustic cochlea response.

## 9. Initial-value problem

The formulation for oscillatory flow in the frequency domain discussed in previous sections can be extended to a general time-dependent response corresponding to an arbitrary time-dependent vibration of the stapes and corresponding vibration of the round window. Assume that the stapes displacement normal to itself is given by $\varepsilon I(\tau)$, where $\tau = \omega t$, the inverse of $\omega$ defines a time scale, and $I(\tau)$ is an arbitrary function. The strength of the point source generating the flow is

$$q(t) = \omega \varepsilon d J(\tau), \tag{94}$$

where $J = \mathrm{d}I/\mathrm{d}\tau$, and $d = A/b$ is the effective length of the stapes footplate.

When the basilar membrane is located at the channel centerline, $y_b = 0$, the counterpart of the integral representation (54) provides us with an expression for the pressure jump across the membrane as a function of position and time,

$$\frac{1}{4\rho}[p](x_0,t) = \int_0^\infty G(x-x_0) f_{tt}(x)\,\mathrm{d}x + \frac{\mathrm{d}q}{\mathrm{d}t}\int_0^\infty G(x-x_0)\frac{\partial}{\partial y}(G(\mathbf{x},\mathbf{x}_{src}) - G(\mathbf{x},\mathbf{x}_{snk}))\,\mathrm{d}x. \tag{95}$$

Combining this equation with the membrane response function (23), substituting (94), and rearranging, we derive the integro-differential equation

$$\begin{aligned}\frac{1}{4\rho\omega^2\varepsilon d}\mathscr{C}(f, f_{xx}, f_{xxxx}, f_t, f_{tt}) = &-\int_0^\infty G(x-x_0)\phi_{\tau\tau}(x)\,\mathrm{d}\hat{x} \\ &-\frac{\mathrm{d}J}{\mathrm{d}\tau}\int_0^\infty G(x-x_0)\frac{\partial}{\partial \hat{y}}(G(\mathbf{x},\mathbf{x}_{src}) - G(\mathbf{x},\mathbf{x}_{snk}))\,\mathrm{d}\hat{x},\end{aligned} \tag{96}$$

where $\phi = f\mathscr{L}/(\varepsilon d)$ is the dimensionless membrane displacement, and $\mathscr{L}$ is a specified length scale. A similar equation was derived by Allen and Sondhi (1979) for a spatially periodic flow model, by Diependaal and Viergever (1989) for the serial cochlear model, and by Mammano and Nobili (1993) and Nobili and Mammano (1996) for more general configurations. The last authors refer to the first and second term on the right-hand side of (96), respectively, as the basilar membrane forcing term and the stapes forcing term, and compute the Green's function for arbitrary geometries by approximation. When $J(\tau) = \exp(\mathrm{i}\tau)$ and $f(x,\tau) = F(x)\exp(\mathrm{i}\tau)$, Eq. (96) reduces to the frequency-domain integral equation (54).

### 9.1. Inertialess membrane

To be more specific, we adopt the membrane response function (24), set the length scale equal to the channel width, $\mathscr{L} = h$, and rearrange to find

$$\int_0^\infty G(x-x_0)\phi_{\tau\tau}(x)\,\mathrm{d}\hat{x} = -\frac{\hat{s}_0}{4\omega^2\beta^2}\,\mathrm{e}^{-\lambda(x-x_r)}(\phi + \omega\beta\phi_\tau) - \frac{\mathrm{d}J}{\mathrm{d}\tau}\int_0^\infty G(x-x_0)\frac{\partial}{\partial\hat{y}}(G(\mathbf{x},\mathbf{x}_{src}) - G(\mathbf{x},\mathbf{x}_{snk}))\,\mathrm{d}\hat{x}. \tag{97}$$

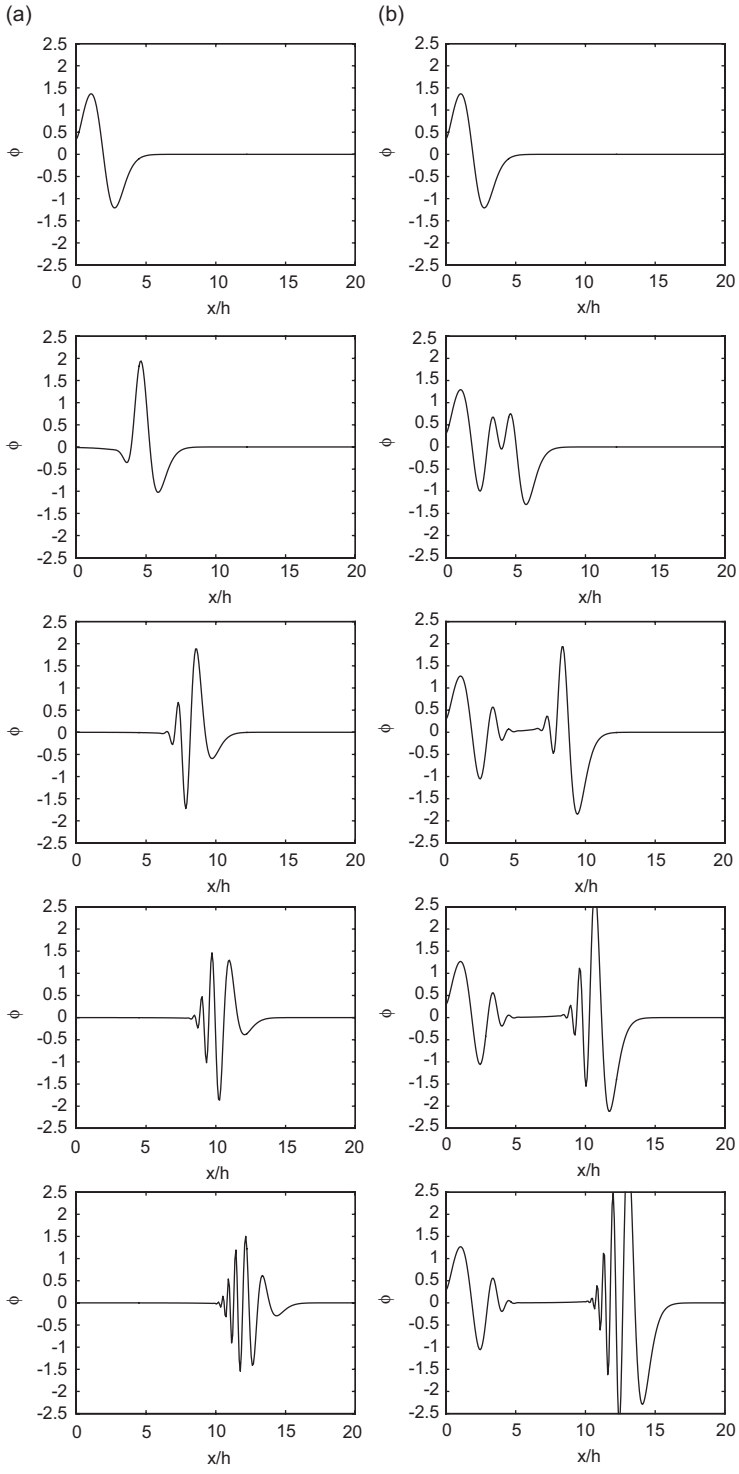


Fig. 16. Transient response of an inertialess membrane for $\omega\beta = 0.5$, $\hat{s}_0 = 2.5 \times 10^{-8}$, $\lambda h = \frac{4}{7}$, and $x_r/h = 30$, at times $\omega t/(2\pi) = 1$, 3, 7, 20 and 35, subject to (a) a single-period sinusoidal impulse, and (b) a persistent sinusoidal forcing applied at the origin of time.

Given $\phi$ and $\phi_\tau$, we obtain an integral equation of the first kind with a weakly singular logarithmic kernel for the acceleration, $\phi_{\tau\tau}$. The solution can be found using the numerical method similar to those described in previous sections, yielding the function

$$\phi_{\tau\tau} = \Phi(\phi, \phi_\tau). \tag{98}$$

The evolving shape of the membrane may then be reconstructed by numerically integrating this second-order linear ordinary differential equation subject to the initial condition $\phi = 0$ and $\phi_\tau = 0$, requiring $J(0) = 0$. In our simulations, we use the second-order Runge–Kutta method.

Fig. 16(a) shows results of a simulation for a single-period sinusoidal impulse described by

$$J(\tau) = \begin{cases} \sin\tau & \text{for } 0<\tau<2\pi, \\ 0 & \text{for } \tau>2\pi. \end{cases} \tag{99}$$

Other parameters are $\omega\beta = 0.5$, $\hat{s}_0 = 2.5\times10^{-8}$, $\lambda h = 4/7$, $x_r/h = 30$, domain truncation level $x/h = 20$, $N = 256$ divisions, and time step $\omega\Delta t = 0.01$. The point source is located at $x_{src} = 0.01h$, $y_{src} = 0.25h$, and the point sink is located at $x_{snk} = 0.01h$, $y_{snk} = -0.25h$. The illustrations reveal the formation of a solitary wave packet consisting of several peaks traveling from the stapes to the helicotrema. The propagation speed decreases as the packet approaches the helicotrema. The frequency content and width of the packet increase, while its amplitude decreases during the propagation.

Fig. 16(b) shows the results of a simulation for the same conditions, but for a permanent sinusoidal forcing function, $J(\tau) = \sin\tau$ for $\tau>0$. The illustrations reveal the formation of a dual wave packet consisting of a time-periodic packet similar to that described in Fig. 7(d) in the frequency domain centered near the stapes, and a traveling packet similar to that described in Fig. 16(a). The second packet is expected to reach the helicotrema and exit the computational domain after a few hundred cycles of oscillation, leaving the stationary wave packet alone. It is interesting that the amplitude of the traveling packet increases during the propagation due to the continuous stapes forcing.

### 9.2. General case

Next, we adopt the general membrane response function (28) and work in similar ways to derive an integral equation of the second kind for $\phi_{\tau\tau}$,

$$\int_0^\infty G(x,x_0)\phi_{\tau\tau}(x)\,\mathrm{d}\hat{x} + \frac{m(x_0)}{4\rho\mathscr{L}}\phi_{\tau\tau} = -\frac{1}{4\rho\mathscr{L}}(c(x_0)\phi + \kappa(x_0)\omega\phi_\tau) - \frac{\mathrm{d}J}{\mathrm{d}\tau}\int_0^\infty G(x,x_0)\frac{\partial}{\partial\hat{y}}(G(\mathbf{x},\mathbf{x}_{src}) - G(\mathbf{x},\mathbf{x}_{snk}))\,\mathrm{d}\hat{x}. \tag{100}$$

The solution for the acceleration, $\phi_{\tau\tau}$, can be found using the numerical methods discussed earlier. We will work with dimensional variables and set the characteristic length scale $\mathscr{L} = 1\,\mathrm{cm}$.

Fig. 17(a) shows the results of a simulation for a single-period sinusoidal impulse with frequency $f = 5\,\mathrm{kHz}$, conducted with domain truncation level $x = 3.5\,\mathrm{cm}$, and $N = 256$ divisions. The snapshots reveal the formation of a traveling wave packet similar to that described in Fig. 16(a). As in the previous case, the frequency content and width of the packet increase, while the amplitude of the packet decreases during the propagation. In this case, it takes approximately 10 ms for the packet to reach the helicotrema. Fig. 17(b) shows the results of a corresponding simulation with a permanent sinusoidal forcing, $J(\tau) = \sin\tau$ for $\tau>0$. The illustrations reveal the formation of a stationary wave packet similar to that described in Fig. 11(a) in the frequency domain, and a traveling wave packet similar to that shown in Fig. 17(a). The amplitude of the traveling packet increases only slightly during the propagation due to the continuous stapes forcing. Physically, the results suggest that the start-up period due to a pure-tone input at 5 kHz lasts for approximately 10 ms. To demonstrate the effect of the length solution domain, in Fig. 17(c) we present a simulation that duplicates that shown in Fig. 17(b) with a longer domain, $L = 5.0\,\mathrm{cm}$. Side-by-side comparison reveals that, while the tail-end of the solution is affected by the solution domain, the general features of the wave train remain the same. Similar results were obtained for a broad range of frequencies.

The counterpart of the integral equation (100) for the serial cochlear model is

$$\int_0^{\hat{L}} \mathscr{G}(x,x_0)\phi_{\tau\tau}(x)\,\mathrm{d}\hat{x} + \frac{m(x_0)}{2\rho\mathscr{L}}\phi_{\tau\tau} = -\frac{1}{2\rho\mathscr{L}}(c(x_0)\phi + \kappa(x_0)\omega\phi_\tau) - \frac{\mathrm{d}J}{\mathrm{d}\tau}\frac{L-x_0}{a}, \tag{101}$$

where the stapes footplate length has been set equal to the scala width, $d = a$. Fig. 18 shows the results of two simulations duplicating those presented in Fig. 17(a), (b). The amplitude of the developing wave packet shown in

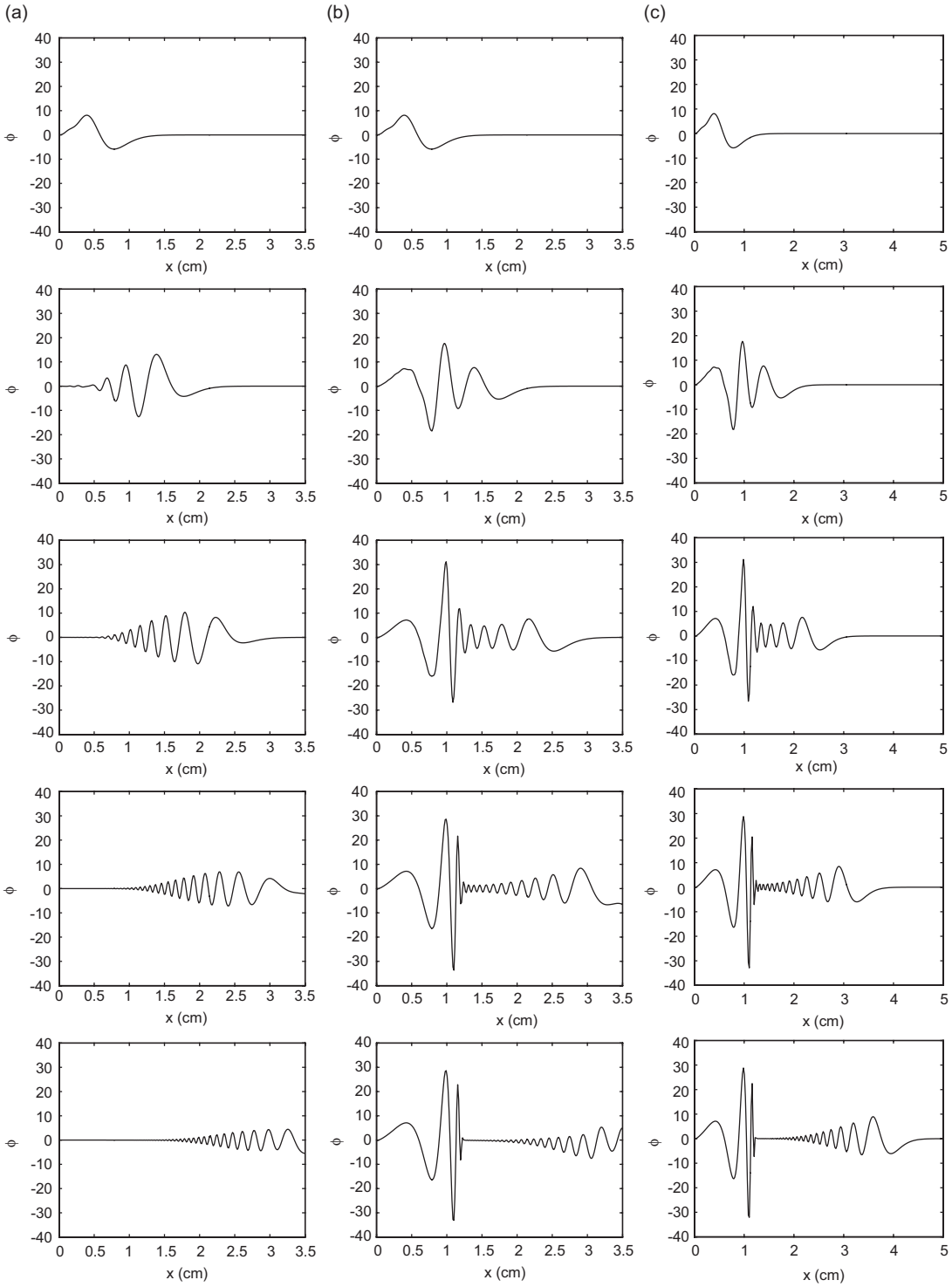


Fig. 17. Traveling and waves at times $ft = 1$, 3, 7, 15 and 30, subject to (a) a single-period sinusoidal impulse, and (b, c) a persistent sinusoidal forcing applied at the origin of time. In both cases, the forcing frequency is $f = 5\,\text{kHz}$.

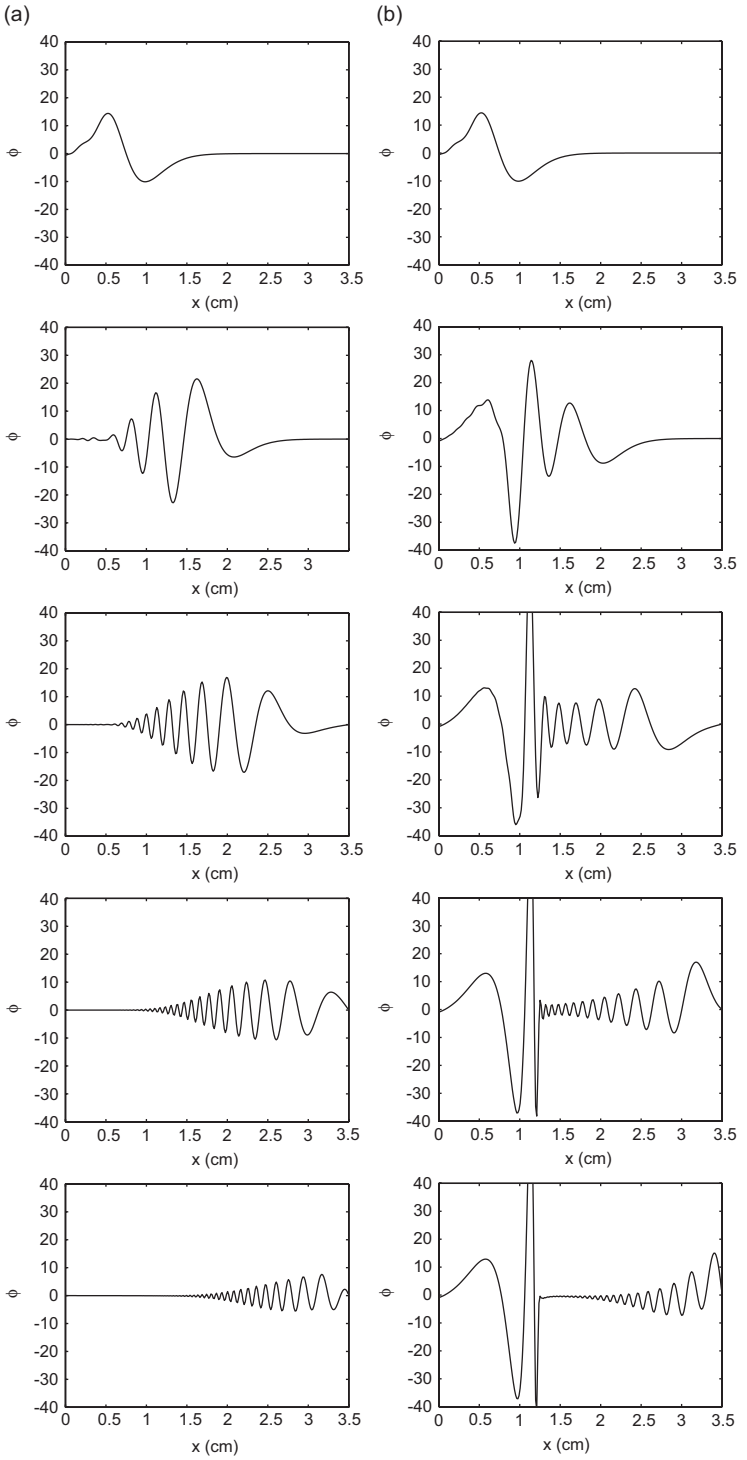


Fig. 18. Same as Fig. 17(a, b), but for the serial cochlear model.

Fig. 18(a) is larger than that shown in Fig. 17(a) due to the stronger action of the stapes and round window. Eventually, the packet disappears as it enters the helicotrema to join its mirror-image on the other side. The transient evolution illustrated in Fig. 18(b) is notably different from that shown in Fig. 17(b), and the approach to the periodic state takes

a much longer time. These comparisons indicate that the precise mechanism driving the flow and the assumed conditions at the helicotrema have a significant influence on the transient vibrations.

## 10. Discussion

We have formulated a two-dimensional cochlear model that uses a point source and a point sink to emulate the action of the stapes footplate and round window, and developed a boundary-integral formulation to describe the induced potential flow and vibration of the basilar membrane. The physical model and integral formulation improve and generalize those developed by previous authors based on the serial cochlear model. The derived integral equations were solved accurately and efficiently using elementary numerical methods to describe the structure of traveling waves on the basilar membrane for an arbitrary membrane response function. The numerical results were confirmed to be consistent with those obtained by previous authors using functional analysis and finite element implementations. The simulations illustrated the detailed structure of the basilar wave packet and demonstrated that the general features of the membrane oscillation are mildly sensitive to the position of the oval and round window and position of the basilar membrane across the cochlear channel.

We have presented results both in the frequency and time domain. In the initial-value problem, the basilar membrane acceleration is found by solving an integral equation whose nature depends on the assumed membrane mechanical response. Numerical solutions for a single-period sinusoidal impulse revealed the formation of a traveling wave packet which eventually disappears at the helicotrema. Numerical solutions for a permanent wave demonstrated the transient dynamics during the initial start-up period.

We have considered passive and linear membrane models where the mechanical properties of the membrane are independent of the basilar membrane vibration amplitude and load, and thus of the excitation of the hair cells residing inside the basilar membrane. It is generally accepted that the passive model cannot explain the extreme sensitivity and frequency selectivity of the cochlea, and it is believed that some kind of internal amplification leading to nonlinear response must take place. Neely and Kim (1983) introduced the first linear active cochlear model expressing negative damping. In their simulations, the membrane oscillations computed from the passive model drive a subordinate spring-mass-damper subsystem representing the response of the stereocilia of the outer hair cells.

More sophisticated models are reviewed by Lim and Steele (2002). In a typical active cochlea model, the balance equation (23) is replaced by

$$p_t(l,t) \equiv [p](l,t) + p_c(l,t) = -\mathscr{C}(f, f_{ll}, f_{llll}, f_t, f_{tt}), \tag{102}$$

where $p_t$ is the total surface force (membrane load), and $p_c$ is an effective downward surface force due to the outer hair cells. The latter can be related to the total membrane load using the relation

$$p_c = \alpha(p_t)p_t, \tag{103}$$

where $\alpha$ is the feed-forward gain factor. Thus,

$$[p] = (1-\alpha)p_t = -(1-\alpha)\mathscr{C}(f, f_{ll}, f_{llll}, f_t, f_{tt}). \tag{104}$$

In the context of the present formulation, implementing an active membrane response results in a system of nonlinear integral equations that must be solved by iterative methods. The study of these active nonlinear systems is under current investigation.

## Acknowledgment

I am indebted to three referees for their constructive comments. This research was supported by a grant provided by the National Science Foundation.

## References

Allen, J.B., 1977. Two-dimensional cochlear fluid model: new results. Journal of the Acoustical Society of America 61, 110–119.

Allen, J.B., Sondhi, M.M., 1979. Cochlear macromechanics: time domain solutions. Journal of the Acoustical Society of America 66, 123–132.

von Békésy, G., 1960. Experiments in Hearing. McGraw–Hill, New York.

Beyer, R.P., 1992. A computational model of the cochlea using the immersed boundary method. Journal of Computational Physics 98, 145–162.

Cai, H., Manoussaki, D., Chadwick, R., 2005. Effects of coiling on the micromechanics of the mammalian cochlea. Journal of the Royal Society Interface 2, 341–348.

Diependaal, R.J., Viergever, M.A., 1989. Nonlinear and active two-dimensional cochlear models: time-domain solution. Journal of the Acoustical Society of America 85, 803–812.

Givelberg, E., Bunn, J., 2003. A comprehensive three-dimensional model of the cochlea. Journal of Computational Physics 191, 377–391.

Kagawa, Y., Yamabuchi, T., Watanabe, N., Mizoguchi, T., 1987. Finite element cochlear models and their steady state. Journal of Sound and Vibration 119, 291–315.

Kolston, P.J., Ashmore, J.F., 1996. Finite element micromechanical modeling of the cochlea in three dimensions. Journal of the Acoustical Society America 99, 455–467.

Lesser, M.B., Berkley, D.A., 1972. Fluid mechanics of the cochlea. Part 1. Journal of Fluid Mechanics 51, 497–512.

LeVeque, R.J., Peskin, C.S., Lax, P., 1985. Solution of a two-dimensional cochlea model using transform techniques. SIAM Journal on Applied Mathematics 45, 450–464.

LeVeque, R.J., Peskin, C.S., Lax, P., 1988. Solution of a two-dimensional cochlea model with fluid viscosity. SIAM Journal on Applied Mathematics 48, 191–213.

Lighthill, J., 1981. Energy flow in the cochlea. Journal of Fluid Mechanics 106, 149–213.

Lim, K., Steele, C.R., 2002. A three-dimensional nonlinear active cochlear model analyzed by the WKB-numeric method. Hearing Research 170, 190–205.

Loh, C.H., 1983. Multiple scale analysis of the spirally coiled cochlea. Journal of the Acoustical Society of America 74, 94–103.

Mammano, F., Nobili, R., 1993. Biophysics of the cochlea: linear approximation. Journal of the Acoustical Society of America 93, 3320–3332.

Manoussaki, D., Chadwick, R.S., 2000. Effects of geometry on fluid loading in a coiled cochlea. SIAM Journal on Applied Mathematics 61, 369–386.

Manoussaki, D., Dimitriadis, E.K., Chadwick, R.S., 2006. Cochleas graded curvature effect on low frequency waves. Physical Review Letters 96, 088701.

Neely, S.T., 1981. Finite difference solution of a two-dimensional mathematical model of the cochlea. Journal of the Acoustical Society of America 69, 1386–1393.

Neely, S.T., Kim, D.O., 1983. An active cochlear model shows sharp tuning and high sensitivity. Hearing Research 9, 123–130.

Nobili, R., Mammano, F., 1996. Biophysics of the cochlea II: stationary nonlinear phenomenology. Journal of the Acoustical Society of America 99, 3320–3332.

Parthasarathi, A.A., Grosh, K., Nuttall, A.L., 2000. Three-dimensional numerical modeling for global cochlear dynamics. Journal of the Acoustical Society of America 107, 474–485.

Pozrikidis, C., 1997. Introduction to Theoretical and Computational Fluid Dynamics. Oxford University Press, New York.

Pozrikidis, C., 2002. A Practical Guide to Boundary Element Methods with the Software Library BEMLIB. Chapman & Hall/CRC Press, Boca Raton.

Rhode, W.S., 1971. Observations of the vibration of the basilar membrane in squirrel monkeys using the Mossbauer technique. Journal of the Acoustical Society of America 49, 1218–1231.

Sondhi, M.M., 1978. Method for computing motion in a two-dimensional cochlear model. Journal of the Acoustical Society of America 63, 1468–1477.

Steele, C.R., Zais, J.G., 1985. Effect of coiling in a cochlear model. Journal of the Acoustical Society of America 77, 1849–1852.

Taber, L.A., Steele, C.R., 1981. Cochlear model including three-dimensional fluid and four models of partition flexibility. Journal of the Acoustical Society of America 70, 426–438.

Viergever, M.A., 1977. A two-dimensional model for the cochlea: II. The heuristic approach and numerical results. Journal of Engineering Mathematics 11, 11–28.

Viergever, M.A., 1978. Basilar membrane motion in a spiral-shaped cochlea. Journal of the Acoustical Society of America 64, 1048–1063.

Viergever, M.A., Kalker, J.J., 1975. A two-dimensional model for the cochlea: I. The exact approach. Journal of Engineering Mathematics 9, 353–365.

Zweig, G., Lipes, II., Pierce, J.H., 1976. The cochlear compromise. Journal of the Acoustical Society of America 59, 975–982.